DESIGN OF A SURFACE ALBEDO MODIFICATION PAYLOAD FOR NEAR EARTH ASTEROID (NEA) MITIGATION

A Thesis

by

SHEN GE

Submitted to the Office of Graduate Studies of
Texas A&M University
in partial fulfillment of the requirements for the degree of

MASTER OF SCIENCE

August 2011

Major Subject: Aerospace Engineering

Design of a Surface Albedo Modification Payload

for Near Earth Asteroid (NEA) Mitigation

DESIGN OF A SURFACE ALBEDO MODIFICATION PAYLOAD FOR NEAR EARTH ASTEROID (NEA) MITIGATION

A Thesis

by

SHEN GE

Submitted to the Office of Graduate Studies of
Texas A&M University
in partial fulfillment of the requirements for the degree of

MASTER OF SCIENCE

Approved by:

Chair of Committee,	David Hyland
Committee Members,	James Turner
	Jim Boyd
	Mehrdad Ehsani
Head of Department,	Dimitris Lagoudas

August 2011

Major Subject: Aerospace Engineering

ABSTRACT

Design of a Surface Albedo Modification Payload

for Near Earth Asteroid (NEA) Mitigation. (August 2011)

Shen Ge, B.S., Georgia Institute of Technology

Chair of Advisory Committee: Dr. David Hyland

The development of the Surface Albedo Treatment System (SATS) onboard a spacecraft mission to the near earth asteroid (NEA) Apophis in 2012 is an innovative concept of deflecting NEAs from possible impact with the Earth through altering the Yarkovsky effect, a non-secular force in the solar system due to uneven surface thermal emission most profoundly affecting small rotating bodies subjected to sunlight. Though this force is small, its magnitude can be dramatic if extended over a period of time and if it uses the close approach of an asteroid near Earth to magnify the perturbation.

The payload dispenses colored powder called albedo changing particles (ACPs) onto the surface changing its albedo and indirectly the surface temperature which changes the Yarkovsky effect. This study gives an in-depth description of both computational and experimental parts of the design of this system with primary focus on initial ground test setup. The initial experiments proposed to design the SATS is outlined in detail and justified by the mission criterion of interest as well as modeling the actual dispersal on the surface.

ACKNOWLEDGEMENTS

I would like to thank Dr. David Hyland for his foresight in seeing this opportunity in Apophis and starting the project on the mitigation technique via the Yarkovsky effect. He has given me helpful insight and the freedom to carry out what was originally just an idea into actual design and experimentation.

Furthermore, much credit goes to his undergraduate students who have been consistently helping out with the overall mission design and assembly of many of the ground experiment components. Lastly, I have to thank the colleagues that have aided me along the way either directly or indirectly in alphabetical order: Darkhan Alimzhanov, Xiaoli Bai, Justin Doyle, Hyerim Kim, Justin Lopez, Richard Margulieux, Julie Sandberg, Neha Satak, and Brian Young.

NOMENCLATURE

A/M	Coverage Mass versus Area Covered Ratio
AC	Albedo Change
ACP	Albedo Changing Particles
ADU	Analog-to-Digital Unit
AO	Atmospheric Oxygen
AU	Astronomical Unit
ETF	Effective Thickness Factor
FF1	Far-field 1
FPTE	First Pass Transfer Efficiency
GCR	Galactic Cosmic Radiation
JPL	Jet Propulsion Laboratory
KACST	King Abdulaziz City for Science and Technology
LEO	Low Earth Orbit
NEA	Near Earth Asteroids
p_{dil}	Dilution Pressure
p_{inj}	Injection Pressure
p_{vor}	Vortex Pressure
PCRG	Powder Coating Research Group
PSD	Particle Size Distribution
Q/M	Charge-mass Ratio

R_A	Asteroid Radius
R_s	Radial Vector from Sun to Asteroid
$R_\oplus$	Earth Radius
SATS	Surface Albedo Treatment System
SEP	Solar Energetic Particles
UTC	Coordinated Universal Time
ρ	Asteroid Density

TABLE OF CONTENTS

Page

LIST OF FIGURES

FIGURE Page

LIST OF TABLES

TABLE Page

1. INTRODUCTION AND MOTIVATION

1.1 Motivation

Near Earth Asteroids (NEAs) such as that of Apophis continually poses a threat to the safety of this planet. Much attention has been spent on the detection and exploration of these pieces of space rock but little has been done in the way of mitigation. Past close planetary encounters have demonstrated the need to have a means to protect Earth. With current estimates, there are over 2000 NEAs with radius larger than 100 km. Detection and exploration are both necessary but what can be done if one of these are found to be on a collision course with Earth?

This thesis addresses this current deficiency through an innovative slow push method through altering the Yarkovsky Effect by changing the surface reflectivity of an asteroid surface. On a deeper note, both simulations and actual ground experiments are currently conducted to develop the payload using the asteroid Apophis as the test case scenario.

This thesis follows the style of Icarus.

1.2 Yarkovsky Effect

The orbital dynamics of NEAs is complicated and affected by a number of forces, most notably gravity. In recent years, there has been growing attention on the importance of a force known as the Yarkovsky Effect. Ivan Osipovich Yarkovsky (1844-1902), a civil engineer who worked on scientific problems in his spare time, first proposed the effect but it was the Estonian astronomer Ernst J. ¨Opik who brought this phenomenon into the public (Bottke et al., 2002).

The Yarkovsky effect is a subtle nongravitational perturbation from the recoil force of anisotropically emitted thermal radiation of a rotating body (Vokrouhlick ́y et al., 2000). For a given surface element of the body, the incoming solar radiation flux in the body-fixed reference frame is modulated by two frequencies: (i) the rotation frequency of the body around an instantaneous spin axis and (ii) the mean-motion frequency that is given by the body's revolution around the Sun. These two frequencies cause the Yarkovsky effect to have both a diurnal component and a seasonal component.

Consider the diurnal component's simplest case. Take a spherical asteroid's spin axis to be normal to the orbital plane so that the Sun is always at its equator (Bottke et al., 2002). Insolation heats up sunward side, with heat ultimately reradiated into space as photons mostly in the infrared range. Each infrared photon carries away a momentum of $p = E/c$ where p is photon's momentum, E its energy, and c is the speed of light. Since more energy departs from the hotter side compared to the colder side, the asteroid feels a net push in a direction opposite of the hot part.

If the asteroid surface has no thermal inertia, the temperature distribution will be

symmetrical about the subsolar point and the net force will be radially outwards from the sun. However, all materials possess thermal inertia, which incurs a delay. This is like on Earth when the hottest time of the day is not at noon but rather the afternoon. Likewise, the hottest part of the asteroid is on the "afternoon" side and not at the subsolar point.

The force on the asteroid has both a radial direction and an along-track direction. The along-track component causes a secular increase in the semimajor axis and the eccentricity for a prograde asteroid shown which leads to a gradual widening of orbit as time goes by. A retrograde rotation will shrink the orbit instead of expanding it. If the rotation axis was on the plane, the diurnal component will not exist at all. Objects with zero or infinite rotation rates experience no diurnal Yarkovsky effect. For rotation periods believed to be typical in the solar system, there is an optimal rotation rate correlated to the size of the asteroid. The best current estimate is the rotation rate of 5 hours for every 1 km diameter.

As stated, the size of the rotating body has a large impact. A large object such as Earth is negligibly affected because it has a very poor area-to-mass ratio, i.e. the amount of force generated on the body is very small compared to the mass of the object. However, if the body is too small, at some point the radius becomes so tiny that there is no longer much of a thermal gradient.

Lastly, the diurnal effect depends on the proximity to the sun, the tilt of the body's spin axis, and other physical characteristics of the body such as its shape and thermal properties. Refer to Figure 1-1 for a schematic.

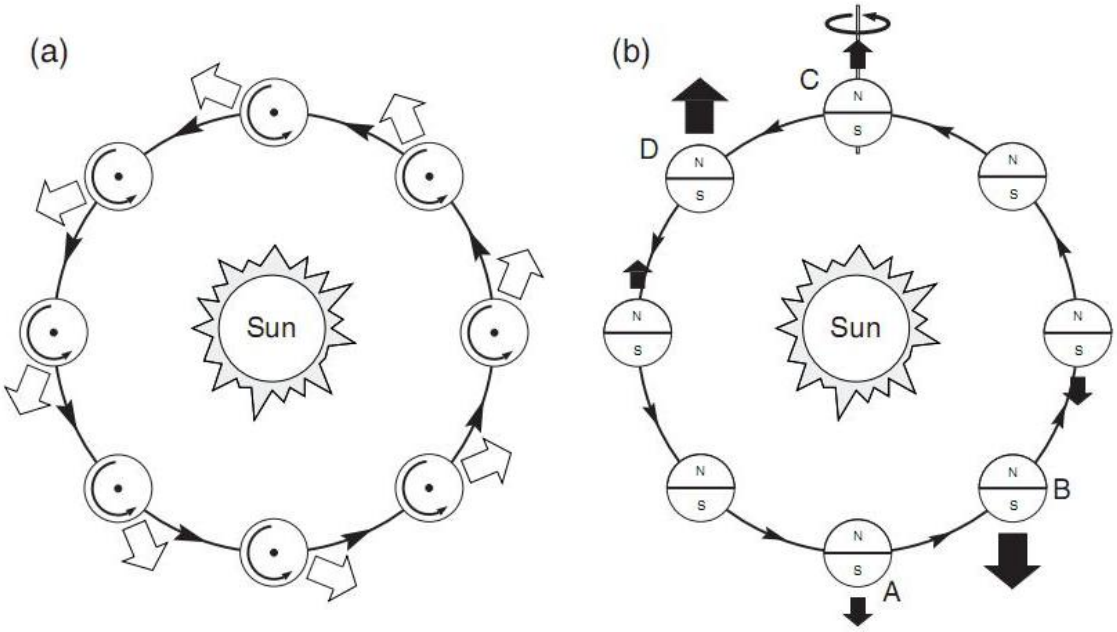

Figure 1-1. Asteroid Subjected to Seasonal Yarkovsky Effect. Schematic of an asteroid around the sun subjected to the Yarkovsky effect.

Nearly a century after Yarkovsky's pamphlet, a second Yarkovsky effect was uncovered to account for the secular decay of the LAGEOS satellite. This second effect is illustrated in Figure 1-1. Once again a spherical asteroid is in orbit around the sun but now the spin axis lies in the orbital plane. When the asteroid is at A, the sun shines most intensely on the northern hemisphere. Like the diurnal effect, there is a delay due to thermal inertia so the northern hemisphere is actually hottest at B. On a similar note, the sun shines most strongly on the southern hemisphere at C but the hemisphere becomes hottest at D. For a body without thermal inertia (an impossible scenario), the along-track

force averages to zero when integrated over one revolution about the sun.

The seasonal Yarkovsky effect always causes orbital decay by creating a retarding along-track force for small orbital eccentricities. Like atmospheric drag, for small eccentricities it tends to circularize the orbit. The seasonal component depends on the proximity to the sun and the tilt of the spin axis with the orbit (vanishing when spin axis is normal to plane). Also like the diurnal case, there is an optimal size to maximize the effect.

1.3 99942 Apophis Characteristics

Though the payload outlined in this thesis can be used for any NEA, special attention has been focused on the asteroid Apophis due to its size and the close-approach opportunity it presents on April 13, 2029 (Schweickart, 2006). When a NEA of particular interest makes a close-approach its period is altered from its relative position to Earth. Essentially, an asteroid passing behind the Earth will be pulled forward approximately along its orbital path, hence lengthening its semi-major axis and thus orbital period. These close encounter episodes also introduce the concept of gravitational resonance and keyholes. A gravitational resonance occurs when for a NEA, after n orbits, its position once again matches that of Earth during which Earth has gone through x orbits. The range of distances from the Earth at the time of close encounter is called the keyhole.

In the case of Apophis, there is a close encounter with Earth on April 13, 2029 which may incur a 7/6 (7 Earth orbits and 6 NEA orbits) resonant return impact on April 13, 2036. Apophis will pass the Earth's center between 5.62 $R_{\oplus}$ and 6.30 $R_{\oplus}$ on Friday,

April 13, 2029 21:45 UTC (Giorgini et al., 2008). An approach this close by an object this large is thought to occur on average once every 800 years. During this encounter, it will be a 3rd magnitude object visible in the night sky. This Apophis keyhole of 2029 is only 600 m wide but if it passes through this keyhole region direct impact will occur exactly 7 years later. JPL studies have originally shown the impact probability in 2036 to be 1 in 45,000 but this probability has dropped to 1 in 250,000 since an updated study at JPL in October, 2010.

Close encounters present the perfect opportunity for slow mitigation techniques due to the dual combination of longer time and smaller necessary momentum transfer. The seven years between close encounter and possible impact allows the slow push or pull from the Yarkovsky effect to accumulate enough displacement while the smaller keyhole size compared to the actual Earth diameter requires several orders less of momentum transfer. This can be seen in the ΔV plot in Figure 1-2 where momentum transfer after 2029 is substantially more costly.

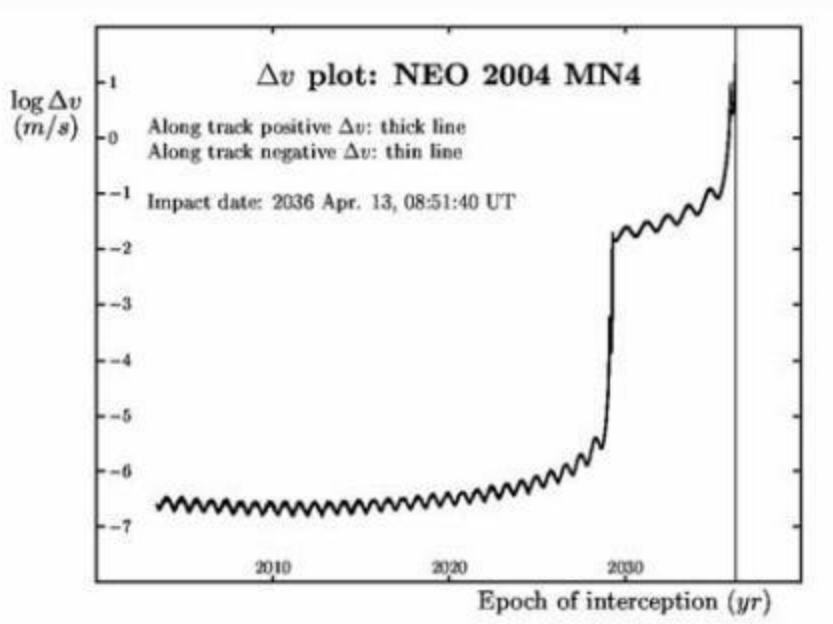

Figure 1-2. Required Deflection Change in Velocity. The required deflection change in velocity necessary after 2029 is 5 orders of magnitude greater than before 2029 (Schweickart, 2006).

Though there has been no spacecraft mission yet to Apophis, there have been a substantial number of Earth-borne observations which through spectral measurements and visual observations combined with modeling techniques have led to some conclusive hypotheses on the physical characteristics of Apophis. It is a Sq-type using categories of Bus taxonomy (Binzel et al., 2009). NEA albedo measurements and survey statistics yielded the possibility of a diameter of 300 meters with an albedo of 0.35. Delbo used direct measurements of albedo 0.33±0.08 along with absolute magnitude (H) of 19.7±0.4 to obtain the best diameter estimate of 270±60 m. Apophis's spectrum modeled using the Shkuratov scattering model can yield an approximation of the mineral composition of Apophis. This can be seen in Table 1-1.

Table 1-1. Mineral Composition of Objects.

OBJECT	OLIVINE (%)	ORTHOPYROXENE	CLINOPYROXENE (%)
H	53	39	8
L	61.5	30.5	8
Apophis	65-75	17-27	3-13
LL	72.5	20	7.5

As can be seen, the estimation techniques done by Binzel et al. show that the spectral characteristics of Apophis most resemble those of LL chondrite meteorites. While the grain density can be approximated with some certainty, an estimate of the total mass has considerable uncertainty as can be seen in Table 1-2.

Table 1-2. Size and Density Estimates of Apophis.

PARAMETER	MIN	AVG	MAX
Apophis Diameter	210 m	270	330
Grain Density	3.4 g/cm^3	3.5	3.6
Bulk Density	3.0 g/cm^3	3.2	3.4
Micro-porosity (%)	3.7	7.9	12.1
Macro-porosity (%)	0	20	50

2. SURFACE ALBEDO TREATMENT SYSTEM

2.1 Introduction

As mentioned previously, the Yarkovsky effect can have a substantial long-term effect on the trajectory of a small body such as that of a NEA like Apophis. Since one of the key criteria affecting the Yarkovsky effect is the thermal distribution of the surface, changing the albedo of the surface should incur a change in this distribution. Albedo is a type of surface reflectivity, more specifically it is defined as the ratio of reflected radiation from surface to incident radiation upon it. Snow has an albedo of 0.9 while asphalt has an albedo of 0.04.

While the modification of albedo via pigmentation has thousands of years of heritage, techniques based on modern industrial powder coating are the most effective way to modify an asteroid surface. A fine powder that can be electrostatically charged and cured to the surface via photoelectric activation gives the most flexibility with the lowest mass, which is a critical factor for a deep-space mission. These albedo changing particles (ACPs) must be designed specifically for such a unique application.

Chondritic bodies such as Apophis have a high electrical resistivity, and their sunlit surfaces accumulate a positive static charge as the solar wind strips away electrons. In addition to the surface charge, this leaves a sheath of negatively charged particles levitated above the surface, as illustrated in Figure 2-1 (Hyland et al., 2009).

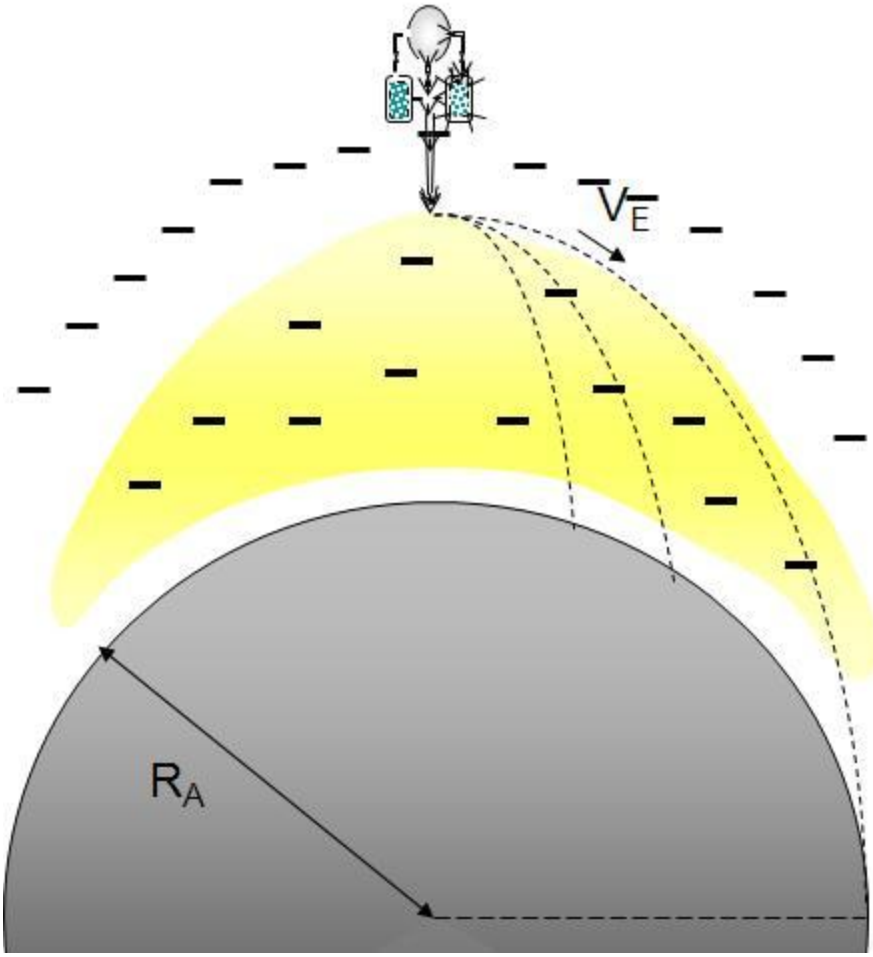

Figure 2-1. Schematic of Spacecraft Around Asteroid.

Because the force of gravity is very small on these kinds of asteroids, simply placing the ACPs on the surface is a challenge. This surface charging provides a solution: by giving the ACPs a negative charge, the particles will be attracted to the surface in the absence of significant gravity. Electrostatic charging is commonly performed in industrial processes by either tribo or corona-charging; tribo-charging, the process of applying a charge through frictional contact between insulators is more suitable for a space-based application due to lower power requirements and the

elimination of high-voltage components.

The tribo-electric dispenser in the Surface Albedo Treatment System (SATS) will use a pressurized inert gas to force the powder through a narrow passageway, where the dispenser wall's material is an electron donor and the ACPs are electron acceptors. The charge acquired by the powder is a function of the materials, configuration, and pressurant application (Dascalescu, 2005, 2009). The pressurant application can be characterized by three factors: the injection, dilution, and vortex pressures. Optimal parameters that maximize the charge gained while minimizing the mass and power required will need to be determined. Numerical models are insufficient for these complex systems, so laboratory equipment capable of testing and varying these factors will be required.

The SATS is composed of four components, as shown in Figure 2-2: the inert gas chamber, ACP chamber, mixing chamber, and tribo-ionization tube.

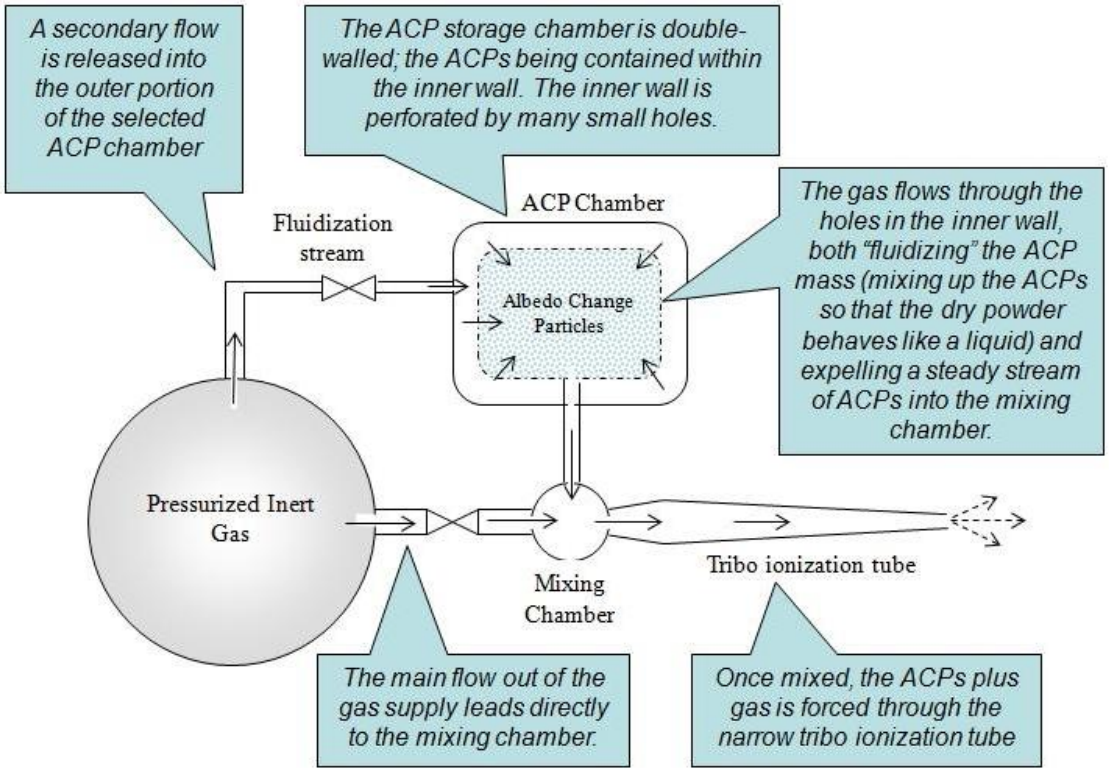

Figure 2-2. Schematic of SATS Payload.

2.2 Structural Design of SATS

Efficiency of electrostatic methods of powder deposition technologies is very strongly correlated to charge/mass ratio from tribocharging (Mihalcioiu, 2005). Maximizing the charge accumulated on the ACPs in the SATS is a key criteria. For a triboelectric dispenser, tribocharging is the source for the charge accumulation. Tribocharging is a collective term for numerous processes of contact charge transfer between solids and liquids.

2.2.1 Tube Material

Charge transfer between two metals via contact is easily derivable from a relation

in their difference of work functions (Supuk et al., 2009). However, contact electrification between a metal and an insulator is much harder to predict. Many researchers assume a triboelectric series which supposedly can predict the charging sign of a particle after contact with a target depending on the insulator's "effective" work function. Ideally, the material higher up the series will always charge positive when in contact with a material lower down the series. However, oftentimes, this is not the case. As of yet, no theory can explain the series quantitatively. Evidently, material-dependent contact charging is only one facet of tribocharging (Poppe and Schrapler, 2005).

The material makeup of the tribodispenser is currently Teflon, which happens to produce positively charged particles. The efficiency of Teflon has been found to charge powders on about the same level as nylon (Mayr and Barringer, 2006). Though ground tests will be necessary to confirm the optimal material for the tribodispenser, the preliminary assumption is to use nylon, a material on the triboseries most prone to donating electrons. Of course, this depends on the material makeup of the powder as well. The ACP will ideally be composed of material mostly on the opposite end of the triboseries.

2.2.2 Tube Length

The length of the dispenser tube is quite important. According to an experiment conducted by Thomas et al., they discovered that the longer the tube is the greater the charge accumulation (Thomas et al., 2007). This can be explained due to greater number of contacts. They found that the charge increases linearly with tube length. However, past a certain length, the charge-to-mass ratio eventually reaches a steady state.

2.2.3 Tube Temperature

Temperature differences between particle and target (the dispenser tube) play a major role in influencing charge transfer according to a study done by Poppe and Schrapler (Poppe and Schrapler, 2005). Reducing target temperature below particle temperature at first reduced charge transfer to a minimum but further cooling it leads to an increase in charge transfer. Alternatively, a higher target temperature than particle temperature increases charge transfer. The dispenser tube may be heated up to a certain optimal temperature by a heater.

2.2.4 Valve Controller

For powder actuation, there are two processes of accomplishing this feat (Biller, 2009). One is using a cold gas thruster setup where there are no active parts. The pressurized vessel is connected to a butterfly valve which is opened whenever the tribodispenser is activated. High pressure naturally pushes the ACPs out of the tube into the tribo dispenser. The other method is using an electric pump which actively pumps the ACPs out of the tube whenever the tribo dispenser is activated. The advantage of the former is simplicity while the advantage of the latter is reliability since any possible tank leakage does not defunct the entire payload.

2.2.5 Pressure Channels and Controller

For a tribocharging device, the charge acquired by the powder can also be modified through the gas pressure (Dascalescu et al., 2008). In order to have greater control of the effect of gas pressure, the gas flow can be divided into multiple channels

entering the triboelectric dispenser at different points. There are three gas circuits as depicted in Figure 2-3 which are the different controls of the system. By adjusting the different pressures in each circuit, the motion of the particles can be changed. The injection pressure p_{inj} affects particle velocity and hence energy of particle impacts; the dilution pressure p_{dil} affects the concentration of powder in the transported air and hence number of impacts; the vortex pressure p_{vor} affects turbulence of motion.

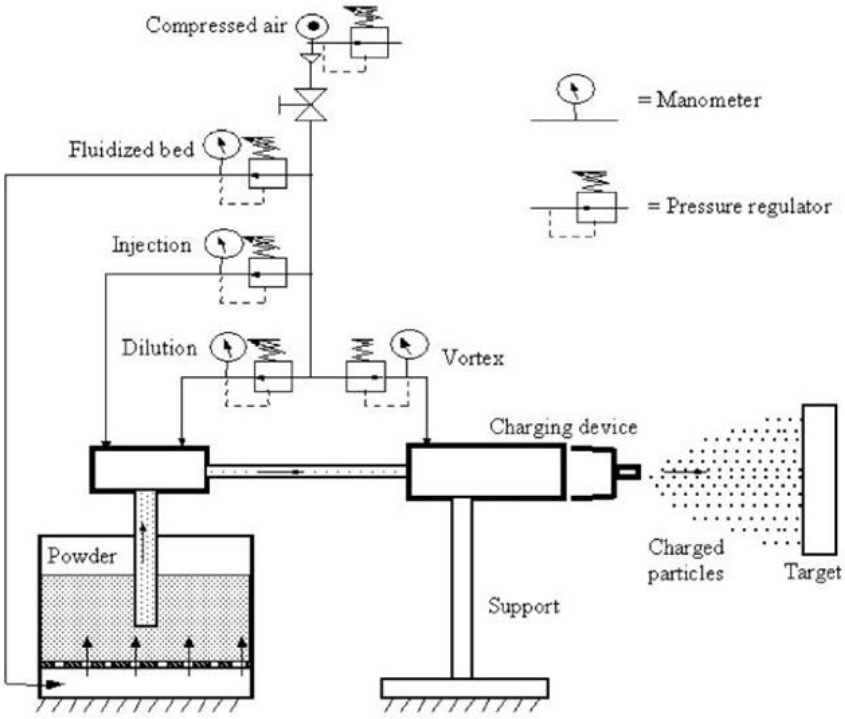

Figure 2-3. Schematic of Pressure Channels of Triboelectric Design.

The range of the pressures for the injection pressure is roughly estimated to be between 140 kPa and 200 kPa. Whether this proves an optimal range in reality will have to be determined in preliminary ground tests.

2.3 Design Requirements of Powder

The requirements for the ACPs to cover the surface have a combination of unique characteristics that current industry powders do not possess. Hence, it is necessary to contract a third party to develop this specialized powder. In this case, consistent correspondence with the Powder Coating Research Group (PCRG) has yielded some interesting properties of the ACP:

- Photoinitiation
- Pigmentation
- Rheology
- Charge
- Size

2.3.1 Photoinitiation

Part of the ACP must be composed of photoinitiators so that the ACP can absorb enough radiation to melt and cure. Conduction with the hot surface is not enough for this to occur. Between the two options of either developing a powder that absorbs infrared or UV light, IR curable powder coatings are easier and less expensive to develop (Biller, 2009). Furthermore, the sun's radiation is 10xs more intense in the IR-visible range than the UV-range. However, the exposure time and temperature of a UV curable powder will influence the fusion, film formation and smoothness so radiation absorption in the UV range should not be neglected.

Curing time and temperature are very closely related in thermosetting powder coating technology (Biller, 2010). This applies to addition cure mechanisms. Some

thermosetting powder coatings use a latent cure mechanism. The proper type and balance of pigments, photoinitiators and oligomers to cure with the expected radiation will be conducted by PCRG. Furthermore PCRG can develop the right blend of oligomers and polymers to melt and fuse under the prevailing conditions expected on the asteroid's surface. The reflectivity and absorptivity of the ACP can be measured in a lab with a spectral photometer.

2.3.2 Pigmentation

Both black and white powders will be needed to have the option of either increasing or decreasing the albedo of the asteroid. Conventional powder coatings, i.e. thermoset powders, are formulated for function and aesthetics; the pigments are incorporated to provide color and opacity. Pigments in a conventional sense are typically more expensive than the binder system. Hence the formulator incorporates the least amount of pigment to provide consistent color at the film thickness the powder is applied. For a very thin film powder a formulator will add more pigment. For a thicker film material less can be incorporated.

Though easy to formulate and mix in with the photoinitiators, concern must be taken on its proportion relative to photoinitiators. Pigments significantly influence the curing of UV curable powder coatings as well as infrared curable powder when the latter is used to melt and fuse the ACPs. It is essential to marry the UV radiation qualities (wavelength, intensity, and dose) of the photoinitiators and pigmentation of the powder coating. The pigments cannot significantly absorb or reflect the UV energy since otherwise the photoinitiators will not absorb enough energy to create the free radicals

necessary to cure the powder binder. Pure white pigments are up to 10% absorptive while for metallic ones, it can be under 10%.

Each pigment has a characteristic opacity. For example, carbon black can be incorporated at 0.5 to 1.0% and provide excellent opacity at 1.0 mil. Titanium dioxide, on the other hand, will have to be added at 40% to achieve similar opacity. UV curable powder coatings are far more complex than the pigment load and film thickness in a thermoset powder. The pigments used in UV powders need to meet opacity requirements while remaining essentially invisible to the UV energy and photoinitiators. The pigment formulating part of the technology will necessarily be more sophisticated.

2.3.3 Rheology

The ACPs must melt, flow, and harden after the absorption of solar radiation and conducive surface temperature. This characteristic to disperse in an opaque film of optimal thickness needs to be thoroughly tested.

2.3.4 Charge

The charge of the ACP will depend substantially on the surface effects and the rate of charge decay. This will be discussed in greater detail under Simulations.

2.3.5 Size

There will be different particle sizes no matter what. Industrial grade powder is about 35-40 micron off from a median particle size (Biller, 2009). Distribution range from 0.5 microns to 90 microns skewed towards the high end. Grinding process produces more big powders. Triboelectric powders typically are between 35-40 microns.

The particle size distribution (PSD) can be performed using a Microtrak Analyzer (Mountain and Mazumder, 2001). This employs an optical diffraction method to find size of particles dispersed in an aqueous medium. Powders are dispersed in a water based medium containing surfactants, using ultrasonic agitation. The details of finding the PSD will be left to PCRG. The PSD will change depending on the duration of fluidization. For the experiment, this will be useful information to know, i.e. the correlation between fluidization time and PSD.

Studies have shown that finer particles increase both coating efficiency and coating uniformity (Li et al., 2005). However, ACP particles must be above a certain diameter in order to counter the phenomenon of dust levitation. According to Lee, the ACP diameter must be above 100 μm to not levitate assuming a distance of 3AU from the sun (Lee, 1996). Given that Apophis will be closer to 1AU where there is more intense solar wind flux and solar radiation causing the dust levitation, it is deemed prudent to go for an ACP diameter of 200 μm.

3. GROUND EXPERIMENT

3.1 Introduction

Before the actual mission to Apophis, multiple experiments must be done near Earth to develop and optimize the SATS. A flight test is planned for a spacecraft orbiting at low-earth orbit (LEO) to test the payload. Before this can be done though, ground experiments must be conducted in a terrestrial lab. The SATS is placed in a controlled environment resembling that of space (more specifically LEO conditions for the ground experiment) from which multiple experiments are done to optimize four parameters. For the full list of equipment and tradeoff studies conducted on tribodispensers and powders, please refer to Appendix B.

3.2 Ground Experiment Setup

3.2.1 SATS Setup

The apparatus is composed of the pressurized gas source, fluidized bed (hopper), a hose connecting the hopper to the mixing chamber, main ionization tube, and nozzle. A schematic of the setup can be seen in Figure 3-1.

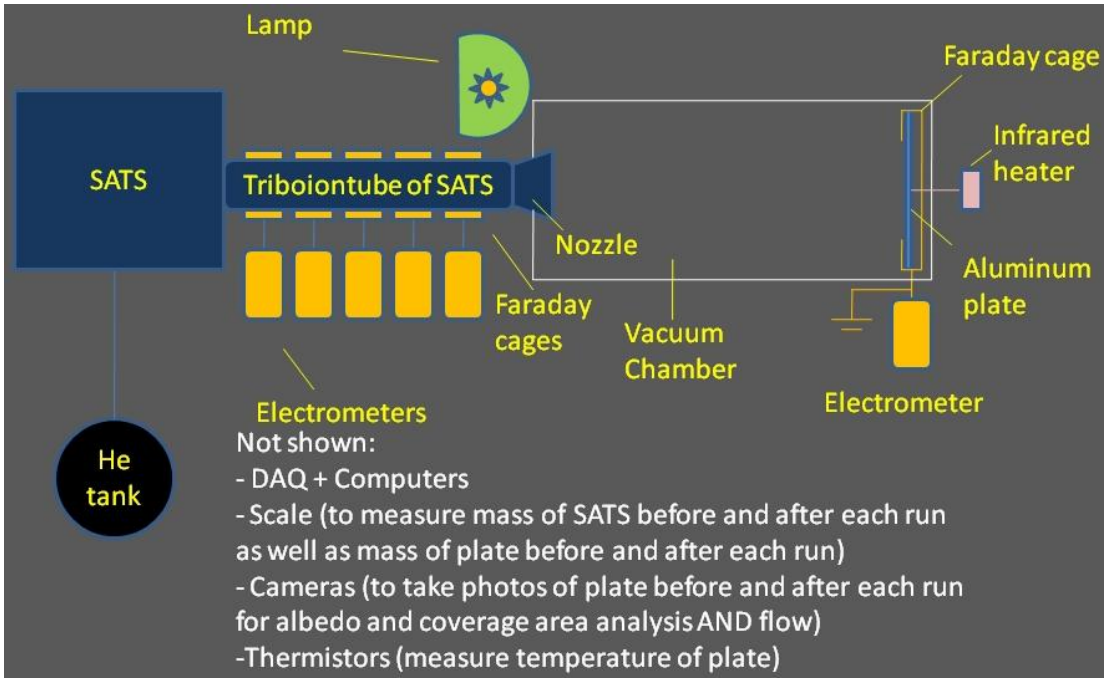

Figure 3-1. Schematic of Ground Experiment Setup.

A fluidized bed of diameter 16 cm and 21 cm can be easily purchased (Mountain and Mazumder, 2001). Its relative humidity needs to be known since that will greatly affect charge transfer. Ideally, a vacuum chamber will be used.

Various gas pressures, lengths, and materials for the tribogun setup must be tested to see a correlation between those variations and the charge/mass ratio. Much can be garnered from Greason's seminal work on triboelectrification between polytetrafluoroethylene (PTFE) and metals (Greason et al., 2004). Though in his experiment, metal pellet balls of 5.5 mm diameter were used, much of his experimental setup can be adopted for our purpose.

A large pressurized neutral gas tank of He_2 is the main gas source depicted in Figure 3-1. A grounded PTFE pipe was attached to the gun's original barrel to extend its length. Pellets were fired horizontally through the pipe enclosed by a Faraday cage and

were collected in the Faraday cup at the end of the pipe. Before each launch, the surface the pipe was swiped with copper brushes to discharge any surface charges by passive discharge elimination. Higher humidity will also help with leaking away excessive charge through moisture film absorbed on the charged surface. Despite this, there's always some residual charge left which can be estimated with this equation

$$Q = Q_0 \exp(-t/\tau)$$

where τ is the time constant of the process. If bulk decay of charges is predominant, then

$$\tau = \rho \varepsilon \varepsilon_0$$

where ε is relative permittivity of PTFE, ε_0 is permittivity of free space ($8.85 * 10^{-12}$ F/m) and ρ is the volume resistivity (mΩ). The time constant can be easily found through just looking at the results of the electrometer and seeing at what time does the charge decrease to 63% of the original charge immediately after particle ejection run.

Another note for "resetting" the pipe is temperature effects. Repeated runs at high velocities will heat up the pipe and increase the charge on the pipe. The temperature inside the pipe can be measured using a 3M laser beam infrared thermometer. Cooling the pipe seems like a good idea if this effect is significant.

The last thing to be noted is cleaning the triboelectric dispenser. This involves a simple blow-out of the tubing and transfer pumps and an inspection of all the parts that come in contact with powder. How this related to a space based unit can be approximated by the estimated amount of powder that will be needed to coat the surface of the asteroid.

3.2.2 Target Generation

The target will initially be flat aluminum plates of uniform roughness and albedo. As the experiment progresses, a surrogate asteroid surface will be constructed emulating that of Apophis's. Though no detailed images of the surface of 99942 Apophis exist, measurements indicate its surface composition to be 65-75% olivine, 17 - 27% ortho-pyroxene, and 3 - 13% clino-pyroxene (Binzel et al., 2009). The test target should be composed of these materials in order to give relative accuracy of the albedo change, as well as particle adhesion and curing for all simulations.

To emulate the surface of Apophis, the test target will consist of several types of terrain ranging from small, granular sized samples to larger, solid rocks. The overall target will be comprised of the appropriate percentage of olivine, ortho-pyroxene, and clino-pyroxene corresponding to the best estimate of the asteroid's composition. These materials may be purchased commercially and will be arranged to emulate the surface of real asteroids.

The asteroid Itokawa is an excellent case to base on given its relatively similar size (Miyamoto et al., 2007). In November 2005, the Hayabusa spacecraft's imaging revealed some rather important details. Grain sizes observed close-up range from centimeters to several tens of meters. The smooth terrains are not randomly distributed on surface of Itokawa with all of them concentrated in areas of low gravitational and rotational potential. There are also small smooth terrains concentrated in local rows such as crater floors. The smooth terrains are homogeneous and featureless with slopes less

than 8◦. Most of the larger gravels are not buried by pebbles, even at their margins while larger particles tend to form clusters.

Keeping those characteristics in mind, the surrogate asteroid surface will be composed of all possible combinations of the types of terrain expected on Apophis. Figure 3-2 shows an example of such an arrangement. The ground experiments will show how effective the ACPs will be for modifying the albedo of any combination of expected terrain.

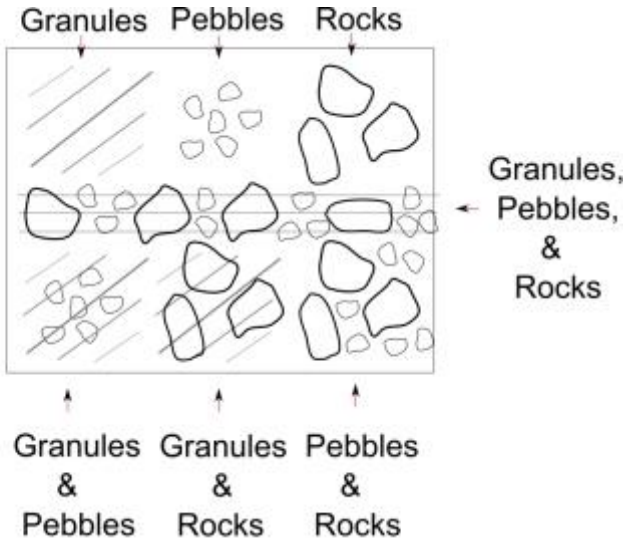

Figure 3-2. Schematic of Test Surface Arrangement.

The ACPs will be directed downwards toward the test surface so that the particles cover most of the target. The different areas of the surface will be analyzed to give insight into how the type of terrain will affect the change in albedo and curing of the particles. Information that may be obtained includes the change in albedo for each separate section of the test bed and the percentage of ACPs that may bounce off the surface and settle outside the target range.

To simulate a more realistic portrayal of surface deposition on an asteroid, a 3D model is also under consideration. Currently, there appears to be two options. The former is to design a 3D model in CAD and use a CNC machine to construct the aluminum model. The alternative is to build a wooden framework, wrap and staple flexible quarter inch wire around it, and then apply plaster to the wire to create a solid surface. In either case, super glue or epoxy can be used to glue the powders and rocks onto the surface. Refer to Figure 3-3 for the latter concept.

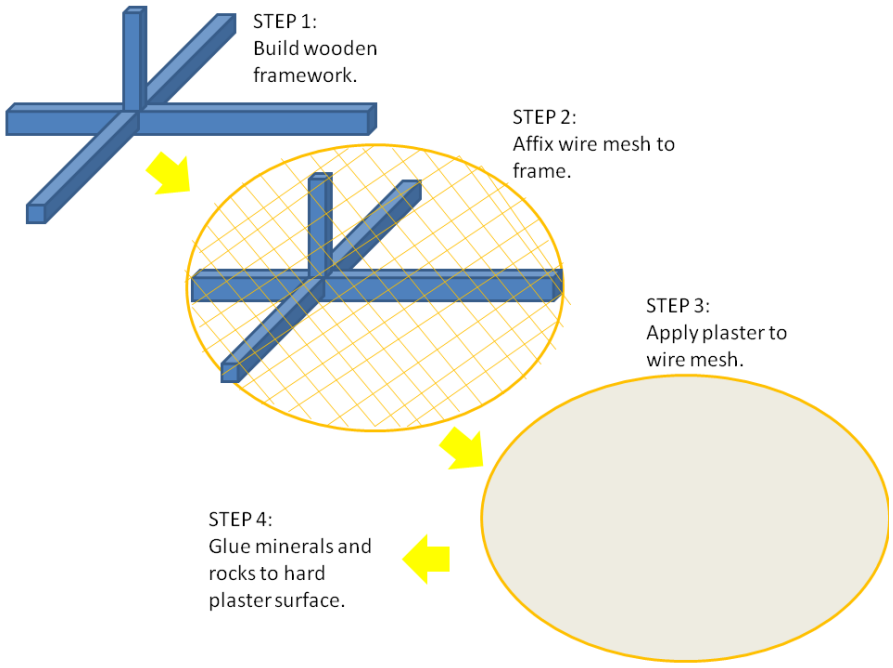

Figure 3-3. Schematic of 3D Surface Construction.

3.2.3 Environment Simulator

The space environment, especially the LEO environment, needs to be carefully simulated by experimental means when possible. An appropriate pressure is of

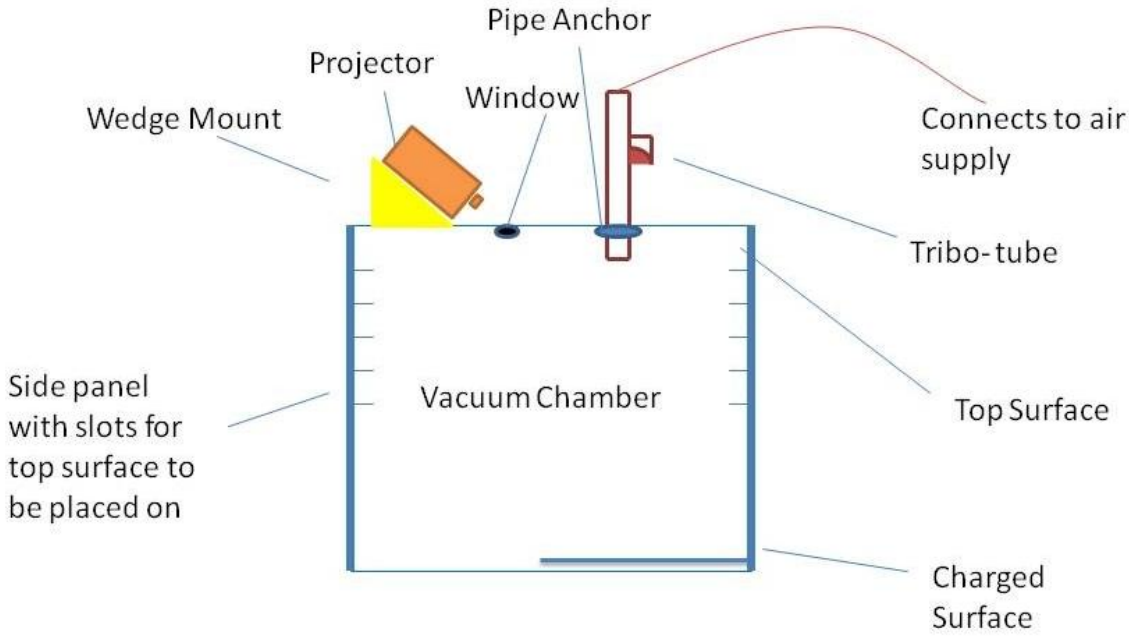

Figure 3-4. Schematic of Side-view of Setup.

penultimate concern. Pressure in space can be defined as the ultra-high vacuum of less than O (10^{-5}) Torr at an altitude of 200 km (Han and Kim, 2006). This ultra-high vacuum state can be simulated via a vacuum chamber that encloses the entire SATS as seen in Figure 3-4. The vacuum created will better simulate the trajectory and charge that the ACPs have without any collisions with air molecules. Outgassing is not considered here since the ACPs are expected to last for a long time.

The next concern is the solar radiation which is necessary for the ACPs to melt and cure. UV to near infrared (NIR) wavelengths (300-4000 nm) is the primary electromagnetic component in the LEO environment for the flight test experiment

(Gueymard, 2004). A projector lamp with known solar spectral properties simulates this solar radiation.

These spectra may have some discrepancy with the spectra from the sun for the actual LEO flight test experiment which implies that all results need to be justified. A few decades of sensors onboard various satellites have proved that the previously used "solar constant" is misnamed because solar energetic outputs vary over time. Instead, total solar irradiance (TSI) should be used. TSI is directly affected by solar activity, which follows the Schwabe (11-year) cycle (Gueymard, 2004). More specifically, more sunspots tend to lower the TSI whereas faculae, plages, and flares tend to increase it. Hence, TSI can vary from one day to the next due to the relative strength and location of these phenomena, which naturally depends on the 27-day solar rotation cycle as well.

Short-term variations are of the same order of magnitude as long-term variations though 27-day amplitudes are usually lower than 11-year amplitudes. The irradiance at different wavelength needs to be compared with theoretical models for solar activity varies and this variation does not influence all wavelengths in same way. The solar irradiance at the edge of atmosphere follows an 11-year solar cycle which naturally has greater UV radiation during periods of greater solar activity (Sola et al., 2007). This ranges from 6 $\pm$1% at 200 nm to lower than 0.5% at 300 nm. Wavelengths longer than 300 nm have variability within the accuracy limit of the instrument, usually 1%. Refer to Figure 3-5 for relative irradiance variations.

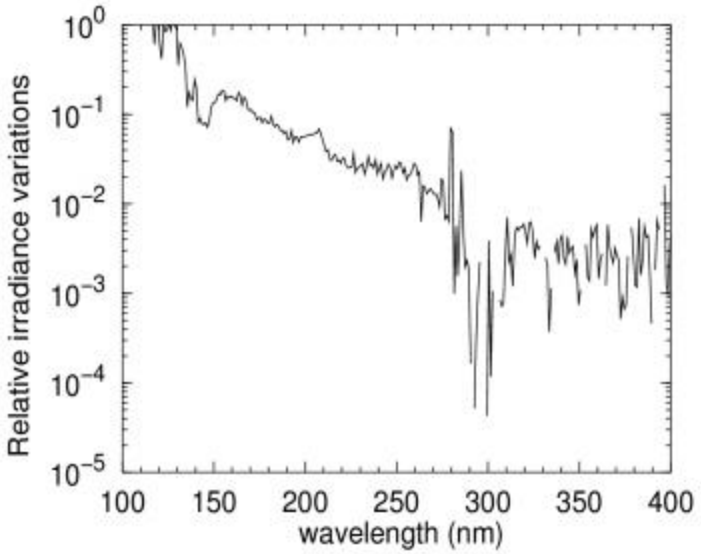

Figure 3-5. Relative Irradiance Variation. Relative irradiance variations between maximum and minimum solar cycle (Sola et al., 2007).

During solar maxima, irradiance with wavelengths less than 240 nm is 30% higher than in minimum period, implying greater production of oxygen. Between the altitudes of 180 to 700 km, atomic oxygen (AO) is the most abundant chemical that can cause major degradation on polymers such as that of ACPs (White et al., 2005). Furthermore, it can cause physical changes and charge transfers. AO is produced from the photodissociation of diatomic oxygen molecules present in the upper atmosphere by solar UV radiation in wavelength range 100-200 nm (Reddy, 1995).

At 300 km, the densities of AO during maximum and minimum solar activities are $8 * 10^{9}$ and $2 * 10^{9}$ atoms/cm^{3}, respectively (Han and Kim, 2006). Although this ambient density is quite low, the orbital speed of the spacecraft ensures high collision energy (Reddy, 1995). If the spacecraft orbits at a velocity of 8 km/s at 300 km, it will

encounter AO particles with kinetic energy of 5eV with nominal AO fluxes ranging from 10^{14} to 10^{15} atoms/cm^2 (Han and Kim, 2006).

AO collision with the surface at this level of energy can initiate a number of different physical and chemical events on the surface. The AO may scatter off the surface in original or altered charged state (Reddy, 1995). It may combine chemically with nitrogen to form nitrogen oxide in its excited state, which de-excites to glow. This glow can interfere with the cameras examining the surface on the spacecraft while the experiment is running. Lastly, degradation can occur when the AO is captured by a potential well at or below the surface to form an oxide. Since AO simulation will require an AO source such as RF and DC plasma sources, ion neutralization, electron-stimulated desorption, photodissociation, supersonic and laser detonation sources that will all cost at least O($10K), its effect is not simulated in the ground experiment. However, it will be accounted for in future simulations.

Aside from AO, there are also three sources of charged-particle radiation in LEO that can cause unwanted charge transfer: galactic cosmic radiation (GCR), trapped radiation belts, and solar energetic particles (SEPs) (Badhwar, 1997). If human spaceflight was considered, they will be also be considered for radiation dosage but here since the spacecraft is unmanned we are only interested in the unit mass charge transfer measured in coulombs per kilogram (C/kg). GCRs emerge from outside the solar system and contain particles of all charges with noticeably hydrogen and helium dominating. The flux of GCRs depend on solar activity; lowest during solar maximum and highest during solar minimum. Earth's magnetic shield allows only a fraction of the incident

flux, depending on the particle's momentum, to reach the spacecraft. Higher orbital inclination allows higher integrated flux to reach the spacecraft. Geomagnetic storms can also have a significant effect.

Trapped radiation belts originating from the Earth's magnetic field contain mostly protons and electrons. If solar activity is kept constant, the flux from proton belts increases nearly exponentially with altitude.

SEPs provide the third source of charged particles in LEO. Strong SEP events occur spontaneously and are impossible to forecast. However, the frequency of such events is a function of solar activity; almost all events occur within a 7-year period around the solar maximum. Nymmik has shown that the number of SEP events per year, N, is a function of the number of sunspots, W, $N = 0.178W^{0.75}$. The peak of the 25th solar cycle is expected to be 2014, with a probable peak sunspot number around 160. These charged-particle radiation effects are difficult to model by ground experiments and must be left to future computer simulations.

3.3 Experimental Methodology

For the experiment, the optimal set of parameters needs to be optimized. These are (1) Albedo change on surface (AC) (2) Average charge/mass ratio of particles (Q/M) (3) First pass transfer efficiency (FPTE) (4) Coverage mass versus area covered ratio (A/M).

AC is the difference between albedo after treatment with the albedo before treatment. This is dependent on the pigmentation of the powder. Q/M is the average charge-to-mass ratio of the particles immediately out of the tube. The charge should be

-10^{-6} Coulombs within 1 standard deviation. FPTE is the ratio of the mass of powder on surface to the total mass of powder ejected. A/M is the ratio of the area of the surface covered with the mass composing the area.

Parameters directly relevant to particles are already set from the specific powder developed before the real ground experiment. These parameters include average particle radius, average particle density, and particle size distribution. However, the dependent variables are dependent on the variation of a large set of independent variables that can have variation. Refer to Table 3-1 for the details.

Table 3-1. Independent-dependent Experimental Variable Correlations.

COMPONENT	Q/M	AC	A/M	FPTE
Tube Length	X		X	X
Tube Material	X			
Tube Radius	X		X	X
Tube Nozzle Design	X	X	X	X
Gas Pressures	X	X	X	X
Particle/Gas Ratio	X	X	X	X
Surface Albedo		X		

Note that these parameters are not mutually exclusive. Indeed, they are related to each other in a complicated manner which only repeated experiments with multiple combinations can optimize. This leads to the issue of the number of experiments to be conducted. Assuming that each independent variable only has two possible choices, classical methodology will still require running 2n number of experiments where n is the number of independent variables. Classical methodology is simply setting one

independent variable constant while adjusting all the other independent variables. In this case, this will mean at least 2^8 or 256 experiments.

A much better alternative is using Taguchi's method to cut down the number of experiments. This method relies on the dependence that is often found between independent variables. For instance, changing the gas pressure will change the particle/gas ratio as well. There is a relation between the two and that means they can be combined as one variable at times. Taguchi's method uses a special set of arrays called orthogonal arrays that outline the minimal number of experiments which can give full information of all factors that affect the performance parameter (Technovision, 2005). Choosing the level combinations of design variables for each independent variable is the key.

The minimum number of experiments required to conduct the Taguchi method can be calculated based on the degrees of freedom.

$$N_{Taguchi} = 1 + \sum_{i=1}^{n} L_i$$

$N_{Taguchi}$ is the number of experiments to run. L_i is the number of possible factors (values) for independent variable *i*. For the simplest case here, there are 15 independent variables with 2 factors each. 8 of factors originate from component variations while the other 7 factors come about from the relationships between the component variations. A linear graph shows the relationships of the variables in Figure 3-6 and Table 3-2.

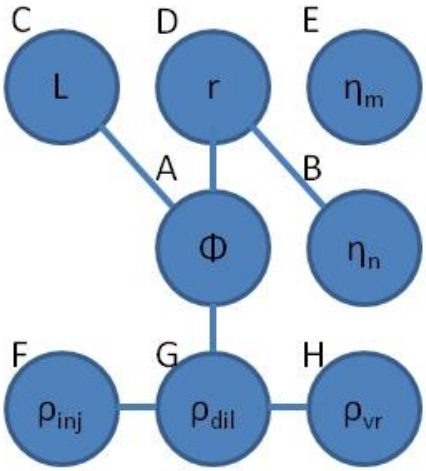

Figure 3-6. Experimental Variable Linear Graph. Experimental variable linear graph outlining relationships.

Table 3-2. Experimental Variable and Choices.

SYMBOL	PARAMETER	SECONDARY VARIABLE	OPTION 1	OPTION 2
L	Tube length	Particle charge	521 mm (default)	1000 mm
R	Tube radius	Mass flow rate	17.5 mm (default)	15 mm
η_m	Tube material	Particle charge	Teflon	Nylon
η_n	Tube nozzle	Particle distribution	Straight	Fan-shaped
Φ	ACP mass	Particle-gas ratio	10 kg	5 kg
ρ_{inj}	Injection pressure	Mass flow rate	140 kPa	200 kPa
ρ_{dil}	Dilution pressure	Particle concentration in gas	110 kPa	170 kPa
ρ_{vor}	Vortex pressure	Turbulence of gas	80 kPa	140 kPa

The orthogonal table L16 with each row outlining the experiment number is outlined in Table 3-3. Note that the letters represent the corresponding independent variables, either physical or relational variables, shown in the linear graph. The column to the furthest right represents the positive or negative error to be added to the experimental variable output.

Table 3-3. Orthogonal Table L16.

T	A	C	AC	D	AD	B	BD	E	F	G	FG	H	GH	AG	e
1	-	-	-	-	-	-	-	-	-	-	-	-	-	-	-
2	-	-	-	-	-	-	-	+	+	+	+	+	+	+	+
3	-	-	-	+	+	+	+	-	-	-	-	+	+	+	+
4	-	-	-	+	+	+	+	+	+	+	+	-	-	-	-
5	-	+	+	-	-	+	+	-	-	+	+	-	-	+	+
6	-	+	+	-	-	+	+	+	+	-	-	+	+	-	-
7	-	+	+	+	+	-	-	-	-	+	+	+	+	-	-
8	-	+	+	+	+	-	-	+	+	-	-	-	-	+	+
9	+	-	+	-	+	-	+	-	+	-	+	-	+	-	+
10	+	-	+	-	+	-	+	+	-	+	-	+	-	+	-
11	+	-	+	+	-	+	-	-	+	-	+	+	-	+	-
12	+	-	+	+	-	+	-	+	-	+	-	-	+	-	+
13	+	+	-	-	+	+	-	-	+	+	-	-	+	+	-
14	+	+	-	-	+	+	-	+	-	-	+	+	-	-	+
15	+	+	-	+	-	-	+	-	+	+	-	+	-	-	+
16	+	+	-	+	-	-	+	+	-	-	+	-	+	+	-

To find the optimal configuration, an equation can be solved for each interested dependent variable (Q/M, AC, FPTE, or A/M) to maximize the value of the dependent variable.

$$y_k = a_0 + \sum_{i=1}^{8} a_i x_i + \sum_{i=1}^{6} a_{i,j} x_i x_j$$

$$a_0 = \sum \frac{y_k}{16} \quad (1)$$

$$a_i = \sum \frac{x_{ik} y_k}{16}$$

where y_k is the kth trial result of output (Q/M, AC, FPTE, or A/M). x_i is either 1 or -1 depending on which input value was chosen for the independent variable. By solving a set of 16 equations for 16 unknowns, the coefficients *a* can be determined. With all *a* determined for a particular output, any output possible for that set of independent variables can be easily computed.

Not all outputs require all 8 physical parameters or their corresponding relational parameters. AC is independent of tube material, radius, or length. A/M and FPTE are independent of tube material. The variables in columns corresponding to the relevant parameters in Table 3-3 are simply deleted in Equation 1.

One particular variable, AC, is dependent on the surface albedo, lending itself to be more easily examined by another means; the surface itself can be a gradient of albedo from light to dark. With appropriate camera setup, one trial will automatically yield the ACP's effects on an entire series of albedos, saving much experimental time.

The possibility that different sets of optimal inputs exist for different outputs is highly likely. To find the "best" option to use, the output parameters must be ranked according to differing weights. An objective hierarchy matrix shown in Table 3-4 yields the results.

Table 3-4. Objective Hierarchy of Output Parameters.

	Q/M	AC	A/M	FPTE
Q/M	1	1/2	3	2
AC	2	1	4	3
A/M	1/3	1/4	1	1/2
FPTE	½	1/3	2	1
Weights	.2771	.4658	.0960	.1611

Each set of outputs from each possible combination of inputs is multiplied by the weights in Table 3-4 to find the combined optimal value. Using Taguchi's method, all 256 sets of outputs can be easily computed after the coefficients in Equation 1 have been

derived. The set of outputs with the greatest combined optimal value correlates to the desired set of inputs.

3.4 Detection Mechanism

3.4.1 Albedo Change

The albedo change is observed through a Nikon SLR camera. To focus the camera on a wider depth of field which is necessary for the wide flat plate area, the lens is attached to a micro tilt adapter to tilt the camera as depicted in Figure 3-7. The imaging process follows as such through the camera-DAQ-computer setup which ultimately produces the final image:

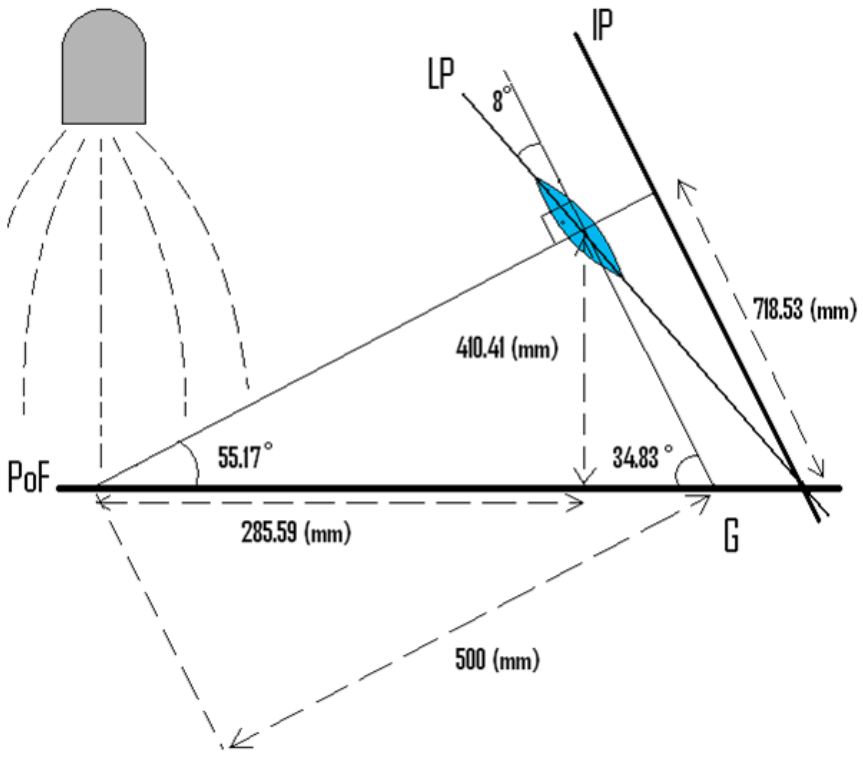

Figure 3-7. Camera and Lens Setup.

1. Projector with known wavelength and intensity illuminates the surface.
2. Use Lambertian reflectance model to predict the reflected radiation.
3. Processed photons through camera are converted to electrons.
4. The electrons create a voltage which is converted to ADUs.
5. Three ADUs (0-255) constitute the grey scale intensity of the pixels for red, green, and blue respectively.

The taken images needed to be converted back to find reflected radiation. The albedo determination process follows the exact opposite route of the imaging process. The steps are shown in Figure 3-8 and are as follows:

1. Red, green, and blue color intensities are combined together to form an 8-bit grey scale matrix.
2. Counts corresponding to each pixel are converted back to voltage through dividing by a gain factor between the number of counts and the number of electrons.
3. The number of electrons is converted to the number of photons through a ratio accounting for sensor quantum efficiency.
4. The photon flux is corrected for lens transmissivity, giving the photon flux before reaching the lens.
5. Knowing the light source can give the number of incident photons. The total flux reflected off the surface and hence the number of reflected photons can be found through the Lambertian model, the direction of the light source, and the flux along the angle that entered the camera.

6. The albedo is found as the ratio between the number of reflected photons and the number of incident photons.

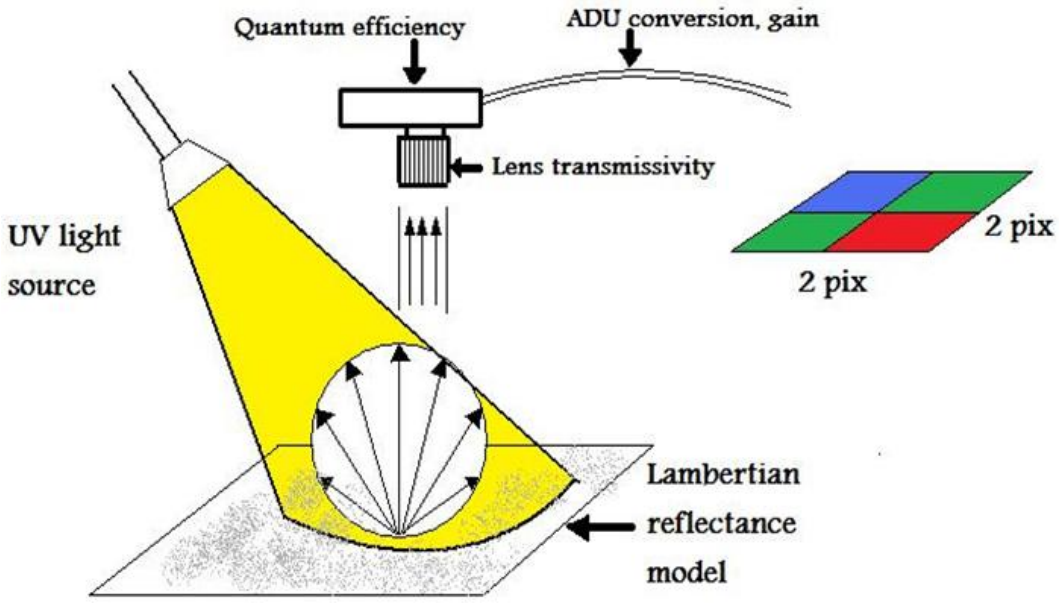

Figure 3-8. Lambertian Reflectance Model for Albedo Detection.

3.4.2 Charge-Mass Ratio

Even before entering the tube, there will be some charges accrued on the powder due to the interactions within the fluidization bed and also the transport hose (Mountain and Mazumder, 2001). When a bed of particles is fluidized by dry gas, the interaction between the opposing flows of particles cause collisions to occur. These particle-to-particle collisions can cause a bipolar charge distribution within the fluidized bed. This is why it's important to connect the fluidized bed to a ground to discharge the high voltage.

Any batch of powder coating is non-homogeneous chemically, i.e. not the same exact amount of polymer backbone, amount of filler and crosslink agent, etc., as well as

non-homogeneous geometrically, i.e. not the same radius or shape (Mountain, 2010). This means that some powders may be more amenable to acquire a positive charge while others are more to acquire a negative charge. Prior to entering the primary triboionization tube, the powder must travel from the bed to the main dispenser through a hose. A distribution of positive and negative particles is assumed to incur.

Greason et al. has found that charge increases with velocity and pipe length (Greason et al., 2004). Intuitively, this makes obvious sense. However, what else they found was more surprising:

1. First region of pipe accumulated largest charge.
2. Middle region accumulated about same charge but lower than first region.
3. Last region accumulated smallest charge.

Furthermore, the dependence of charge on particle speed also changed in different parts of the tube:

1. First region has the charge strongly positively correlated to velocity of the particle.
2. Middle region has particle charge having little relation with the velocity.
3. Last region has particle change actually decrease with increased velocity.

For an inexplicable reason, the charge observed on the tube was 3-5 times greater than those measured for the particles. This has important consequences for how long it's necessary to wait for the pipe to discharge. Clearly, there is an optimum pipe length and velocity combination (dependent on gas pressure) that will produce the maximum charge.

To measure the charge, an open-ended Faraday cage can statically measure total electrical charge acquired through dispenser tube (Thomas et al., 2007). The Faraday cup used to measure the charge is comprised of two metal cylinders with the open end facing the gun. The inner cylinder is connected to an electrometer while the outer one is grounded.

In addition, there is also an alternate setup with multiple Faraday cages of equal length distributed along the span of the pipe (Dascalescu et al., 2010). Each Faraday cage is connected to an electrometer which can measure the amount of charge that the tube loses or gains. The Faraday cages are formed from grounded metallic cylinders coaxial with the pipe and shields each probe from external electric fields. BNC cables that act as probes connect to the adhesive aluminum tapes which wraps around Teflon tapes. Coulombmeters or electrometers in coulombmeter mode connect to aluminum tapes via the BNC cables. A charge amplifier may be employed if readings are too low (Murane et al., 1996). Presumably, the charge on the pipe will be equal in magnitude to that of the particles. In other words, there are two different ways of measuring charge: measuring the particle charge directly or measuring the pipe charge.

If cost is not a consideration, measuring the pipe charge presents advantages since it is non-intrusive allowing the flow to be undisturbed. The details of the parts necessary are depicted in Figure 3-9.

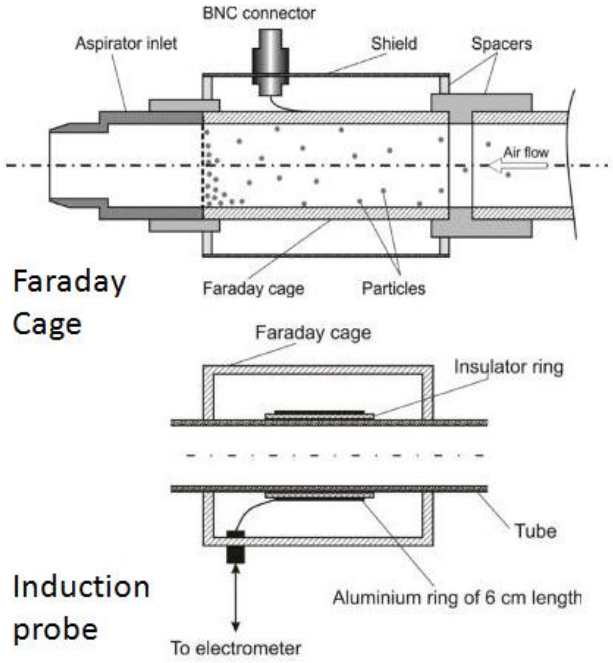

Figure 3-9. Schematic of Non-intrusive Charge Detection.

3.4.3 FPTE and Coverage Area over Mass

Different operating parameters such as airflow rate, powder spray rate, particle size, etc. can have a substantial effect on the first pass transfer efficiency (FPTE) (Shah et al., 2005). FPTE is the ratio of powder deposited on coating target to amount of powder injected from powder spray gun. FPTE and uniformity of the coating layer can be taken as the best parameters to measure performance of coating process. Uniformity of the coating layer can be done through an effective thickness factor (ETF). ETF is defined as the ratio of actual powder mass required to cover between 85%-98% of the coating area and the total powder mass on the coating area. This ratio will obviously be below 1 since there will always be an uneven distribution where certain areas are more concentrated. The true performance is hence EFPTE = FPTE x ETF.

The FPTE can be calculated based on using a scale to measure the mass removed from the powder hopper and comparing that with the mass gained on the surface. The latter will also be used for the coverage area over mass ratio. The coverage area can be found by using a computer imaging algorithm to be coded combined with the camera to tell how much of the area has changed.

4. PARTICLE SIMULATOR

Optimizing the design of the triboelectric dispenser requires some prior knowledge of the parameter ranges that the dispenser should perform at such as optimal particle velocity to maximize coverage. These parameters can be estimated through a full range of simulations that can simulate the path of particles from the interior of the tribodispenser to its behavior on the surface. The simulations can be divided into three zones: near-field, far-field, and on the surface.

The near-field focuses on modeling in Fluent of charge accumulation and particle dynamics within the dispenser from the fluid flow and wall impacts. According to Shah, smaller size particles are influenced more by airflow while larger particles are influenced more by gravity. Shah found that 35 μm particles deflect more sideways as they leave the gun tip due to deflector while 15 μm follow a straighter route.

The far-field focuses on particle dynamics in the region between the spacecraft and the asteroid surface. On the surface focuses on curing and charging due to gravitation and radiation after landing on the surface. Primary focus will be on the far-field effects here.

The primary design parameters of interest in the far-field simulation are the inputs from the near-field simulation, i.e. the mass (or density), radius, and charge of the ACPs as they leave the near-field region. These design parameters must be adjusted to achieve the maximum albedo change on the surface. The other design parameter of interest is the spacecraft height. All other parameters are from the external

environmental and they are varied because of their uncertainty which affects the design parameters.

The mass of the ACPs necessary to deflect Apophis by 2036 can be found through Equation 2 (Hyland et al., 2009).

$$M_T = \frac{\pi R^2 w \rho_p \|\Delta x\|_{2036}}{\Gamma \|\alpha_T/\alpha_0 - 1\| R_\oplus} \tag{2}$$

The ranges for the various inputs of the equation are shown in Table 4-1.

Table 4-1. Mass Calculations of ACPs.

Variable	Quantity	Description
Radius of Apophis	R	105 - $165\ m$
Density of ACP	ρ_p	$1.78\ g/cm^3$
Surface Thickness	w	$50\ \mu m$
Distance from Orbital Track by 2036	$\|\Delta x\|_{2036}$	$3R_\oplus$
Geometric Albedo of Treated Surface	α_T	$0.1 - 0.9$
Bond Albedo	α_0	$0.1383 - 0.1613$
Orbit Sensitivity Factor	Γ	$200 - 1450$

Assuming that the geometric albedo of treated surface is 0.9, the most sensitive case requires 1.2 kg while the least-sensitive case requires 28 kg. This means an equivalent $1.55 * 10^8$ ACPs and $3.76 * 10^9$ ACPs respectively for the most-sensitive case and least-sensitive case respectively. The ensuing simulations assume a nominal radius of 135 m for the asteroid which requires 3.8 kg or $5.1 * 10^8$ ACPs. Since the calculation time required to propagate the equations of motion for such a quantity of particles is exorbitant, only 1000 ACPs are propagated in the Monte Carlo simulations.

4.1 Far-field 1 (FF-1): Interspace Simulator

After leaving the dense plasma cloud in the vicinity close to the spacecraft, the ACPs travel through a vacuum. In this interspace region, there are various forces which affect the motion of the particles. The primary inputs as well as variability are outlined in Table 4-2.

Table 4-2. Parameters and Values of Spacecraft and Asteroid.

Parameter	Symbol	Value
Physical Dynamics		
Mass of Apophis	M	$0.7 * 10^{10}$ - $6.1 * 10^{10}$ kg
Radius of Apophis	R	105 - 165 m
Rotational Period	ω	30.5 hrs
Surface Charge Density	σ	$1.87 * 10^{-22} C/m^2$
Density of ACP	ρ_p	1.78 g/cm^3
Diameter of ACP	D_p	200 μm
Charge-Mass Ratio of ACP	q_m	.0232 C/kg
Plasma Sheath Height	h_p	$1m$
Design Choices		
Spacecraft Height	h	50 - 150 m
Initial Velocity	$\dot{r}$	3 - 12 cm/s

Some of the parameters have single defined values while others are given the flexibility of a range of values. The range of values exists due to two reasons: inherent uncertainty of the dynamics and design choices. In either case, the simulations are run for different combinations of these ranged parameters.

The values of parameters for Apophis were mostly from literature review, specifically through Binzel et al.'s work. Due to measurement errors from ground-based observations, there currently exists a wide range of possibilities of Apophis's dynamics.

Surface charge density was estimated from Lee's model (Lee, 1996). The equation for surface charge density can be estimated by Equation 3.

$$\sigma = n_0 L_{pe} \tag{3}$$

where n_0 is the photoelectron density in the subsolar region while L_{pe} is the Debye length of the photoelectron sheath at 1 AU. The photoelectron density is estimated by Equation 4.

$$n_0 = \frac{2F_0 Y_{pe}}{v_0} \tag{4}$$

Y_{pe} = 0.1 is the photoelectron quantum yield estimated from the best current estimate of the photoelectric properties of asteroid surfaces. v_0 is the average electron emission velocity $7.8 * 10^5$ m/s estimated from assuming photons of near 8 eV and allowing for a work function of order of a few eV for the surface. F_0 is the integrated flux in photons/m^2/s at the subsolar point which can be estimated based on a ratio. Considering that Lee has calculated $n_{0,3AU}$ to be $1.3 * 10^{-3}$ photons/m^3 and $F_0 \propto 1/d^2$ where d is the distance from the sun to the asteroid, using rearranged Equation 4 can yield Equation 5.

$$F_{0,1AU} = 9\frac{n_0 v_0}{2Y_{pe}} \tag{5}$$

The integrated flux at 1 AU is simply 9x larger than Lee's calculation which also applies to n_0. This gives $1.17 * 10^{-2}$ photons/m^3. The Debye length L_{pe} at 1 AU is

estimated similarly based on a ratio knowing the photoelectron density n_0 and L_{pe}, at 3AU = 0.3 m. Equation 6 shows the ratio derived.

$$L_{pe} = L_{pe,3AU}\sqrt{\frac{n_{0,3AU}}{9 * n_{0,3AU}}} \tag{6}$$

This yields Lpe = 0.1m at 1 AU which combined with n0 = $1.17 * 10^{-2}$ photons/m^3 gives the surface charge density σ of $1.87 * 10^{-22}$ C/m2. The diameter of ACP was based on Lee's work which showed that though smaller radii naturally have better surface volume/surface area ratio, there reaches a point when small particles are easily levitated on the surface of an asteroid (Lee, 1996). Finally, note that the composition of the ACP has not been defined yet; the density of ACP was based on that of the Kynar ADX 100.

There were a number of parameter values that could not be definitively defined until the near-field simulation outputs are established; hence, their ranges were defined on some preliminary models. The velocity range must be defined according to an Interspace simulator using a guessed charge for the ACP. This will be discussed in greater detail later in this section. With the particle velocity range established, the range of ACP charge-mass ratio accumulated after going through the tribodispenser tube needs to be calculated.

For metal-insulator interactions, there is a formula derived by Dekker given in Equation 7 which offers an estimate of the surface charge density (Supuk et al., 2009). However, that's assuming the tube is metallic which may be invalid.

$$\sigma = 1.77x10^{-9}\epsilon[(\phi_M - \phi_I)/\lambda \tag{7}$$

φ_M is the work function of metal and φ_I is "effective" work function of insulator. is the dielectric constant of insulator and λ is electron affinity. Note though that for insulator-insulator interactions, there is no magic formula. The triboelectric series is not always right and there's no theory to even explain the order of the series. However, there is a definite maximum charge each particle can hold and equally importantly charge does decay after a certain amount of time (Cheever, 1975). This is quite important since we want sufficient charge so that by the time it touches the surface, the charge is still non-zero. There must be a minimum charge starting out from the triboelectric dispenser desired.

Instead of using Equation 7, a more accurate option is to derive the charge-mass ratio based on the assumptions of the other design parameters. Finding this minimum charge-mass ratio may require several iterations changing different design parameters assuming the initial setup of the other design parameters is inadequate to generate enough charge.

The charge-mass ratio can be derived based on Komatsu's model of static electrification of solids in a gas flow. Though his study did not include an interior solid core, his model was helpful in giving a preliminary guideline on expected charge-mass ratio for following simulations (Komatsu et al., 1976). Assuming a number of assumptions given in Table 4-3, a series of equations are used to give a preliminary estimate of the charge-mass ratio for the ACP.

Table 4-3. Charge-mass Ratio of ACPs.

Parameter	Symbol	Value
Dependent Variables		
Charge-mass Ratio	q/m_p	.0232 C/kg
Charge-mass Ratio (max)	$q/m_{p,max}$	.0290 C/kg
Relaxation Number	n_0	97.36
Collision Function	$n(x)$	157.9
ACP-Gas Mass Flow Ratio	m	248.3
Area of Contact	S	$3.142 * 10^{-11} m^2$
Duration of Contact	Δt	$1.290s$
Independent Variables		
Dielectric Constant	ϵ_0	$8.85 * 10^{-12} F/m$
Depth of Deformed Part	d	0.001
Particle Diameter	D_p	$200\mu m$
Density of Gas	ρ_a	1.1839 (air) or 0.164 (He) kg/m^3
Density of ACP	ρ_p	$1780 kg/m^3$
Gas Velocity	u	$0.1m/s$
Average Gas Velocity	$\overline{u}$	$0.12m/s$
Axial Component of ACP Velocity	v	$0.12m/s$
Average Axial Component of ACP Velocity	$\overline{v}$	$0.12m/s$
Diameter of Pipe (interior)	D	$0.019m$
Relaxation Time	τ	$4.5s$
Contact Potential Difference	V_c	$2V$
Gap between Contact Bodies	z_0	$5 * 10^{-10} m$

The equation for the charge-mass ratio is given by Equation 8.

$$q/m_p = q/m_{p,max}[1 - e^{\frac{-n(x)}{n_0}} \tag{8}$$

Note that Equation 8 depends on three other equations which can be estimated by Equations 9, 10, and 11.

$$q/m_{p,max} = \frac{\frac{3\epsilon_0 V_c}{\rho_p D_p z_0}}{1 + \frac{3m\rho a D u}{\rho_p D p \overline{v}}} \tag{9}$$

$$n_0 = \frac{\pi D_p^2/2S}{(1 + \frac{3m\rho a D u}{\rho_p D p \overline{v}})(1 - e^{-\Delta t/\tau})} \tag{10}$$

$$n(x) = \frac{10x}{D} \tag{11}$$

Note that the collision function in Equation 11 is based on the assumption that the number of collisions increase linearly with relation to the length of the tube and inversely proportional to the diameter of the tube. The factor 10 assumes turbulence to increase the collision rate.

Note that there are several constants that must also be calculated, notably the coverage surface area, S, and the ACP mass-gas flow ratio, m. S is based on the assumption that the ACP deforms to an extent of 0.1% of the original diameter. *m* is calculated from the ratio between an assumed powder mass flow rate and the geometric and physical constraints of the tube size and flow rate. They are given by equations 12 and 13.

$$S = \pi D_p d \tag{12}$$

$$m = \frac{W}{\pi D^2 \rho_a \overline{u}} \tag{13}$$

This new charge/mass ratio was plugged back into the original Interspace simulator to simulate the dynamics once more. The outputs of this far-field trajectory simulator are substituted as the inputs of the Plasma Sheath simulator to confirm their effectiveness as will be described in the next section. If found to be ineffective, the charge/mass ratio will be increased by a magnitude and the entire process repeated.

The primary forces are from the asteroid's gravity (gravitational), asteroid's surface potential (electrostatics), and solar radiation (thermal) (Burns, 1979). The gravitational force is

$$\overrightarrow{F_g} = \frac{GMm}{r^3}\overrightarrow{r} \tag{14}$$

where G is the gravitational constant defined to be $6.67*10^{-11}$ $m^3/kg/s^2$, M is the mass of Apophis, m is the mass of the ACP, r is the distance between the mass centers of Apophis and the ACP (at initial time r is just spacecraft height h), and r is the displacement of the ACP in Cartesian coordinates. Equation 15 shows the electrostatic force:

$$\overrightarrow{F_e} = q\sum\sum\frac{\sigma A}{r^3}\overrightarrow{r} \tag{15}$$

where q is the charge of the ACP in Coulombs (C), σ is the surface charge density of Apophis in C/m^2, and A is the incremental surface area, assumed to be 1 m^2. Equation 16 shows solar radiation force:

$$\overrightarrow{F_r} = \frac{SA}{c}Q_{pr}[(1-\frac{v}{c})\hat{S} - \frac{\overrightarrow{v}}{c}] \tag{16}$$

where S is the solar flux of 1367 $W/m^2/s$, A is the ACP surface area, c is the speed of light, and v is the velocity of the ACP. Q_{pr} is the radiation pressure coefficient and assumed to be 1, i.e. ACP is assumed to be an ideal radiation absorber. The direction of S is assumed to lie antiparallel to the z-axis which means there is no contribution from the first term in Equation 16 for the x and y directions.

Interspace simulation uses basic Newton-Euler equations and integration via numerical Runge-Kutta method with an incremented time step of $\Delta t = 5$ seconds to propagate positions and velocities. Assume an initial velocity and zero acceleration. When the powders reach the position of a height hp above the asteroid surface, the outputs of FF1 are passed to Far-field 2 (FF2). Note the effect of solar wind charging the ACPs in this region has been ignored.

Though direct Monte Carlo simulation can certainly yield results, the computational time is restrictive. Since this system is deterministic with a given input velocity and direction, a more simple and efficient approach will be to find the final positions on the surface with its respective probability given certain set of inputs. The velocity magnitude is assumed to be uniformly distributed between 3 cm/s and 12 cm/s while the velocity angular direction in the z-plane, φ, varies in a normal distribution with the mean at the center, i.e. directed directly downwards. The normal distribution for the angle φ is assumed to have a standard deviation of $\pi/6$ to give a probability range as shown in the schematic of Figure 4-1.

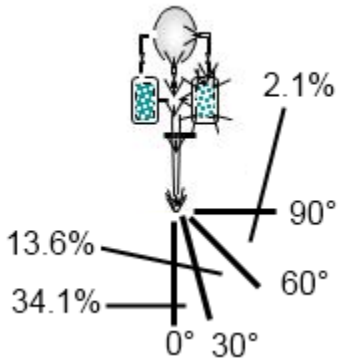

Figure 4-1. Schematic of Velocity Angular Directions. Also includes respective probabilities.

The output of these velocity magnitudes and directions at the assumed sheath height, 1 m above surface, are shown in Appendix A for the cases of spacecraft altitudes of 150 m for Apophis radius of 105 m, 135 m, and 165 m.

4.1.1 Results

This technique also gives the range of velocities allowed which will not have particles touch the plasma sheath. Given a run time of 5000 s, any ACP that has not reached the radial distance of 136 m (sum of Apophis nominal radius and the sheath height) by that time is considered invalid. 5000 s is the time required for an ACP ejected at minimum velocity of 3 cm/s downwards to traverse 150 m. Tables A-1 through A-3 in Appendix A shows the positions of the ACPs at the end of the run time assuming an initial altitude of 150 m.

Note that there is also a variation on the xy-plane but since that angular distribution θ is assumed to be uniform and the asteroid model is assumed to have no variation across the xy-plane, for purposes of showing a representative sample of contact points, $\theta = 0$.

4.2 Far-field 1 (FF-2): Plasma Sheath Simulator

The current model assumes a spherical geometry and uniform surface charge for the asteroid; the effects of solar wind on particle charge will be neglected. The model takes into account three possible outcomes when encountering a plasma sheath expected to hover above the surface of Apophis; this layer consists of negatively-charged particles and may deter the ACPs from reaching the target surface (Nitter and Havnes, 1992).

When the particles enter the sheath, they may either continue toward the surface, be deflected and never reach the surface, or become suspended in this charged layer. To ensure that the first alternative is achieved, the ACP input parameters must be tuned. These variable inputs are outlined in Table 4-4. Other constants that are uncertain also play a role but they are assumed to be a defined value for simulation simplicity.

The Debye length is a key parameter here in that it defines the minimum distance scale over which the particles may be considered in its collective behavior (Lee, 1996). Any distance smaller than this will have to consider interactions between individual particles. There are two sources of particle interaction at work here and both need to be examined for their spatial scales. For solar wind, at 1 AU the Debye length is 12 m. For the near-surface electron cloud, at 1 AU the Debye length is 0.1 m. The more significant Debye length is the shorter one.

Table 4-4. Parameters and Values in FF-2 equations.

Parameter	Symbol	Value
Constants		
Boltzmann Constant	k	$1.38 * 10^{-23} J/K$
Electron Temperature	T_e	$1.5 * 10^5 K$
Permittivity of Free Space	ϵ_0	$8.85 * 10^{-12} F/m$
Mass of Electron	m_e	$9.11 * 10^{-31} kg$
Charge of Electron	e	$1.6 * 10^{-19} C$
Mass of Proton	m_i	$1.67 * 10^{-27} kg$
Electron/Ion Density in Free Space	n_0	$5 * 10^6 electrons/m^3$
Debye Length	λ_d	$0.1m$
ACP radius	a	$100\mu m$
ACP mass	m_d	$7.46 * 10^{-9} kg$
Gravitational Constant	g	$0.1m/s^2$
Radius of Apophis	R	$135\ m$
Sheath Thickness	h_z	$1\ m$
Physical Dynamics		
Solar Wind Mach Number	M	$1-5$
Plasma Sheath Potential	V	$(-)1-(-)5V$
Design Choices		
Initial Acceleration	$\ddot{r}$	FF1 output
Initial Velocity	$\dot{r}$	FF1 output

The plasma sheath height is the height above the surface where the simulation for FF2 begins and FF1 ends. The plasma sheath thickness is the radial distance through which the dynamics of FF2 applies. Assuming a spherical geometry for the asteroid, the position, velocity, and acceleration outputs in Cartesian coordinates from FF1 can be converted to that of spherical coordinates for input into FF2. Since FF2 equations only take into account the radial direction, for simplicity's sake, the ACP trajectory will be assumed to only change radially. Any acceleration and velocity along the azimuth or polar angles will be assumed to be 0.

The conversion from Cartesian to spherical coordinates can be given by Equation 17.

$$\begin{aligned} r &= \sqrt{x^2+y^2+z^2}, r \in [0,\pi) \\ \theta &= \arctan y/x, \theta \in [0,2\pi) \\ \phi &= \arccos z/r, \phi \in [0,\pi) \end{aligned} \tag{17}$$

There are three equations to be solved to acquire radial dynamics versus time. *z* is the normalized radial position. *Y* is the normalized potential of the plasma sheath. Y_d is the normalized relative potential of the ACP surface. These can be solved by using several non-dimensional variables as given by Equation 18.

$$\begin{aligned} Y &= eV/kT_e \\ z &= (R+h_p)/\lambda_d \\ Y_d &= eU/kT_e \end{aligned} \tag{18}$$

Equation 21 for *Y* can be solved independently of the other equations knowing a few boundary conditions. The plasma potential, *Y*, will vary depending on the radial distance from the surface.

$$\frac{1}{2}\left(\frac{dY}{dz}\right)^2 = M^2\left[\left(1-\frac{2Y}{M^2}\right)^{1/2}-1\right]+e^Y-1 \tag{19}$$

$$Y(\pm\infty) = 0 \tag{20}$$

$$Y(0) = -2.84 + ln(M) \tag{21}$$

For the ACP normalized potential, Y_d is based on the electron, I_e, and ion, I_i, current in the plasma sheath. These can be found based on Equations 23 and 24.

$$\frac{dY_d}{dt} = \frac{e}{4\pi\epsilon_0 akT_e}(I_e + I_i) \tag{22}$$

$$I_e = \begin{cases} -n_0 e\pi a^2 \sqrt{\frac{8kT_e}{\pi m_e}} e^Y e^{Y_d} & \text{if } U \leq 0 \\ -n_0 e\pi a^2 \sqrt{\frac{8kT_e}{\pi m_e}} e^Y e^{1+Yd} & \text{otherwise} \end{cases} \tag{23}$$

$$I_i = n_0 e\pi a^2 M(\frac{kT_e}{m_i})^{1/2}(1 - \frac{2eY_d}{M^2 - 2Y} \tag{24}$$

The force equation is given by Equation 25 and must be solved simultaneously with Equation 22.

$$m_d\lambda_d\frac{d^2z}{dt^2} = -4\pi a(\epsilon_0 n_0 e)^{1/2}(\frac{kT_e}{e})^{3/2}Y_d\frac{dY}{dz} - m_d g \tag{25}$$

Estimates of *Y* at various *z* can be substituted in the set of Equations 22 and 25 to solve for *z* as a function of time. After 30 seconds of simulation time, the ACP radial positions at t_{final} are examined to determine whether particles have landed on the surface. Following the probabilistic approach mentioned earlier, only particles with velocities that touched the sheath will be used as inputs here.

4.2.1 Results

As in FF1, there are a number of ACPs that do not reach the surface. These input velocities are too slow or in the wrong direction to penetrate the plasma sheath. Like before, three cases of asteroid radii of 105 m, 135 m, and 165 m are examined. The solar wind Mach number and the normalized potential are varied accordingly. The initial

velocities at the end of the tribodispenser and the final *x, y, z* positions for the θ and φ in the spacecraft frame is shown in Appendix A.

In many cases, no particles land at the surface. We will only look at the ones that do. Considering that the nadir of the spacecraft is z = 0, concentric distances from that point can be found to give an estimate of the likelihood of particles landing areas. Since there are found to be little variations in landing spots between varying Mach numbers and normalized potentials, Figures 4-2, 4-3, 4-4 show variations in ACP dispersal locations between altitudes for the different scenarios examined.

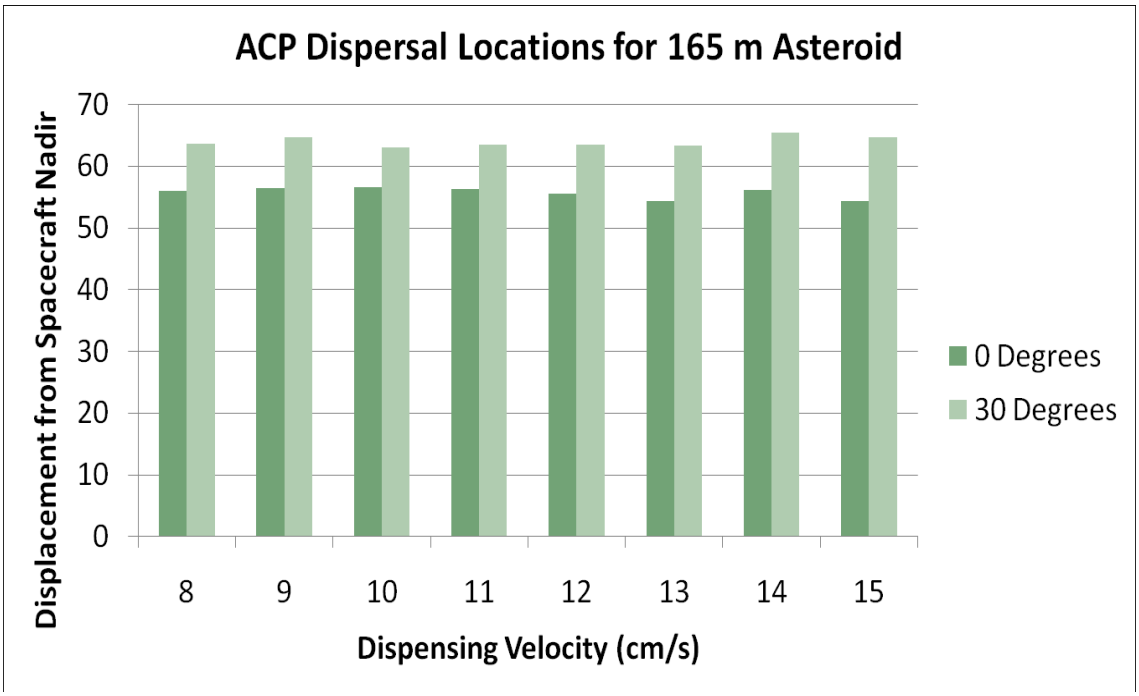

Figure 4-2. ACP Dispersal Locations vs. Initial Velocity (165 m Radius) Plot.

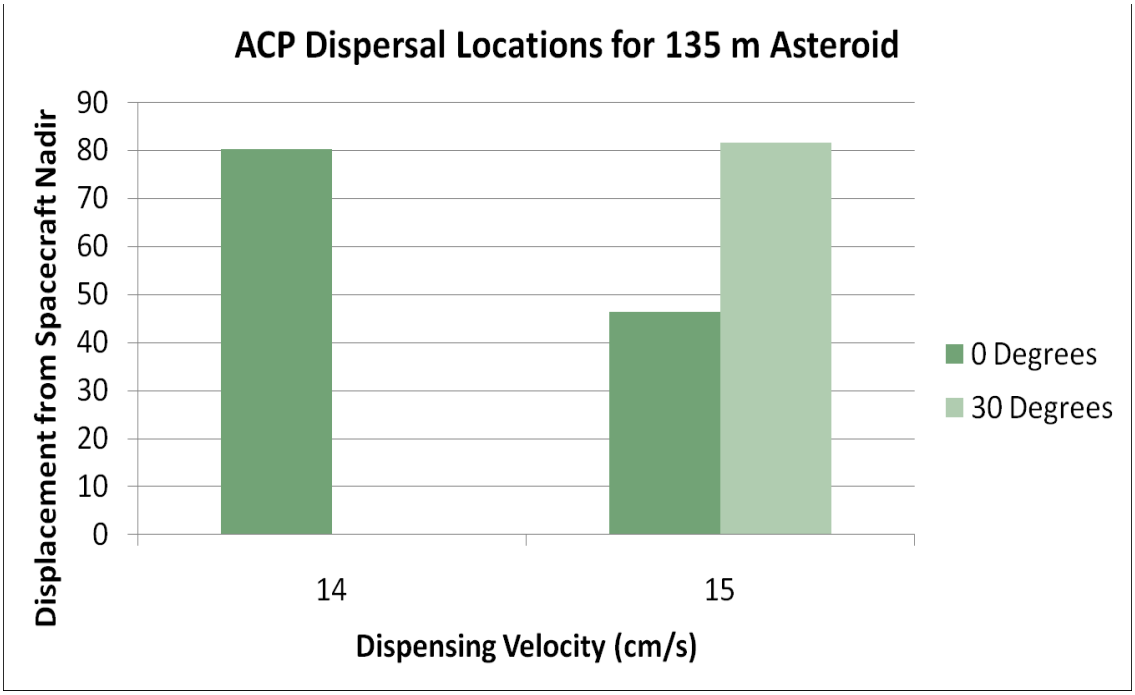

Figure 4-3. ACP Dispersal Locations vs. Initial Velocity (135 m Radius) Plot.

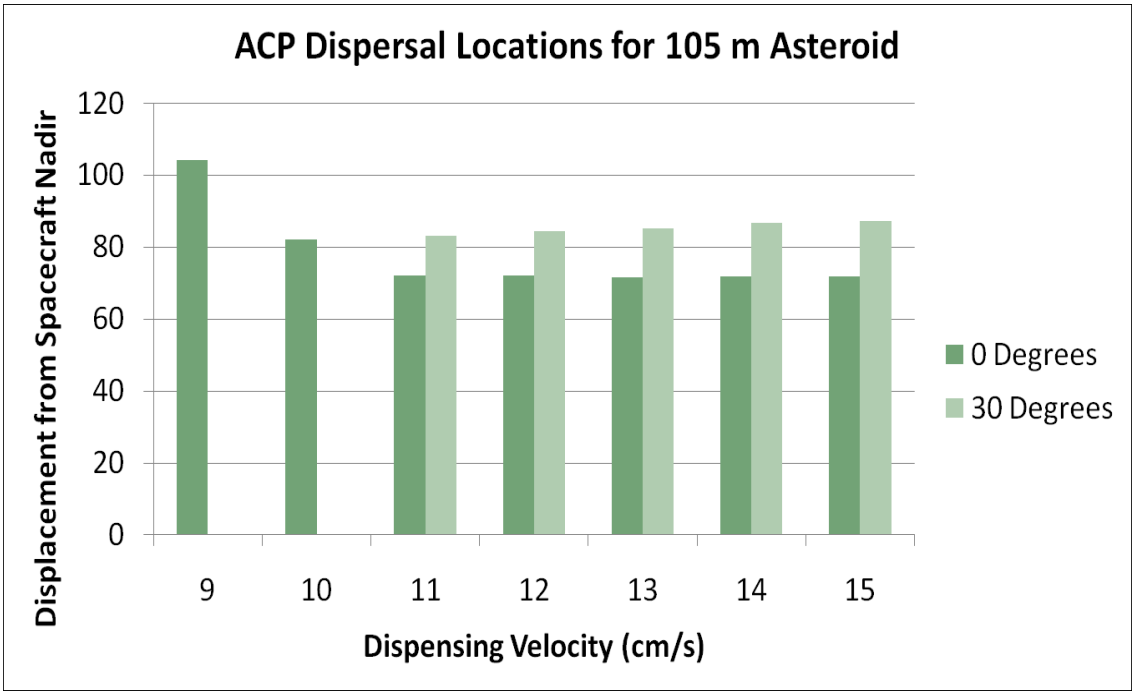

Figure 4-4. ACP Dispersal Locations vs. Initial Velocity (105 m Radius) Plot.

As can be seen, for a 150 m spacecraft altitude, to go through the sheath and to land on the surface, the optimal dispensing speeds are 11-15 cm/s for 105 m asteroid, 14-15 cm/s for 135 m asteroid, and 8-15 cm/s for 165 m asteroid.

4.3 Surface Effects

The outputs will be coverage depth, coverage area, and albedo change as distributed throughout the target surface. Statistical results may be achieved from the collected information, and image analysis aids in quantifying the results. Note that the asteroid will be rotating below the spacecraft so as to produce a band around. The terrain hardiness will affect the dynamics through inducing the particle to possibly bounce or not. The terrain albedo affects imaging since a dark surface undergoes a larger effect when covered with a light powder when compared with a lighter surface that gets the same treatment. Furthermore, shadowed regions are negatively charged which will affect the dynamics of the ACPs differently from sunlit regions. The terrain height also affects the dynamics through impacts at different times and different angles of recoil from the surface.

The amount of change in albedo from pre-treatment to post-treatment can be examined for a variety of random asteroid surfaces to give an idea of the number of ACPs necessary to effect .5% change in albedo of the surface area. The simulation can be best summarized in these steps:

1. Create a realistic needle map n(i, j) of the surface where (i, j) is a particular pixel in the MxN image matrix. A needle map is just a matrix of normal vectors to the surface.

2. Assume a solar position relative to the surface. This determines the direction of the lighting.
3. Create an intensity map of an asteroid.
4. Find the geometric albedo at every pixel by assuming a Lambertian model.
5. Find the bond albedo function number through some assumptions of the relations between albedo and a model. Also, find the total bond albedo for the entire observed sunlit region.
6. Apply the ACP positions from the outputs of FF2 for both colors. Find the amount of albedo change detected for either case. Correlate it with the bond albedo function number and the total albedo.

4.3.1 Needle Map

The needle map is a matrix of normal vectors at every point on the asteroid surface. Considering that this model uses a spherical asteroid, finding the global needle map is relatively trivial. First, the latitudes and longitudes are found through λ = arctan r/z and θ = arctan y/x respectively where r = $\sqrt{x^2 + y^2}$

The normal vector is then found through Equation 26.

$$\begin{aligned} N_x &= \cos\lambda\cos\theta \\ N_y &= \cos\lambda\sin\theta \\ N_z &= \sin\lambda \end{aligned} \tag{26}$$

Since there are mountains and craters on the surface, local normal vectors are also found. The local normal vector depends on the specific terrain of the mountain or

crater. An altitude profile is randomly chosen for each mountain or crater. These included the following types:

1. Constant slope
2. Half-spherical slope
3. Quadratic hill/crater
4. Gaussian hill/crater

These local normal vectors are found through localized ’latitude’ and ’longitude’ coordinates similar to before. The local normal vectors are then added to the global normal vectors to acquire the normal vector.

4.3.2 Solar Position

The solar position ˆ s is given as a unit vector representing the direction of the light source. Here, the vector from the light source to the asteroid surface is assumed to be [0 0 1].

4.3.3 Intensity Map

The intensity map is a matrix of intensities of the image from 0 to 1. This is generated by creating a mesh grid of uniformly random intensities of size 270 X 270. Here, each pixel depicts 1m. Aside from possible ACP clumping when the ACPs are initially ejected from the tribodispenser, ACP landing positions are dispersed far enough where this distance is reasonable. The intensity is defined within a certain range by setting a maximum and a minimum intensity. There are also a number of random craters, mountains, and grooves on the asteroid surface. The craters and mountains are generated

by ellipses of various sizes and rotations with random intensities that either increase or decrease from the center point. The intensity increase or decrease is modeled by a Gaussian. The grooves are generated by random jagged lines of various lengths with random intensities. Refer to Figure 4-5 for a depiction.

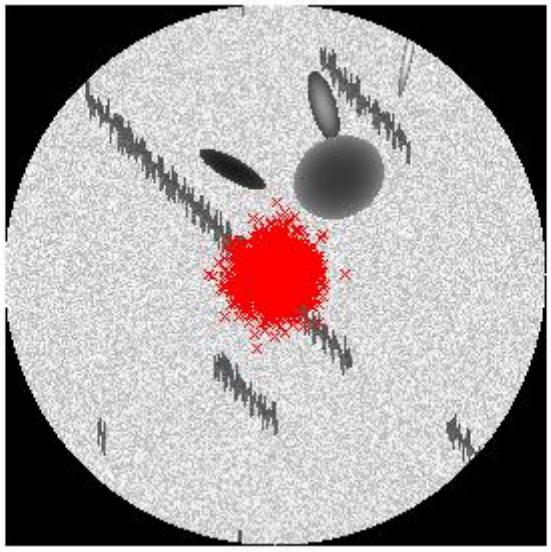

Figure 4-5. Intensity Map of Spherical Asteroid (135 m Radius). Each pixel representing 1 m.

4.3.4 Geometric Albedo

The geometric albedo at any particular location (i, j) can be related to the intensity at that point I(i, j) through a simple ratio as seen in Equation 27 (Smith and Hancock, 2005).

$$\rho_v(i,j) = \frac{I(i,j)}{n(i,j)\cdot\hat{s}} \tag{27}$$

Since all parameters are already known, ρ(i, j) at every pixel of the image can be easily computed.

4.3.5 Bond Albedo and Weighted Bond Albedo

The bond albedo is the albedo taking into account all possible angles of the light initially hitting the surface. The bond albedo A can be related to the measured albedo ρ_v through the ratio $A = q\rho_v$ where q is the phase integral (Giorgini et al., 2008). The phase integral q is found through numerical integration to be $q = 0.290+0.684G$ where $0 \leq G \leq 1$. If the slope parameter G is assumed 0.25, for moderate-albedo Sq class objects the q for Apophis is 0.461.

Though it may seem reasonable to use the white ACP if the bond albedo is low and the black ACP if the bond albedo is high, due to the probability distribution of particle positions, if the lower albedo regions are distributed closer to the point directly below the spacecraft, using high albedo ACPs may be more of an advantage due to the greater likelihood of concentration there.

4.3.6 Results

A normal probability distribution from the nadir is used as the basis of generating the total number of ACPs distributed as such on the surface using the case of the nominal radius of 135 m and a spacecraft altitude of 150 m. Assuming a landing distribution with standard deviation of 20 m, with 500000 ACPs, three scenarios for asteroid surface images are taken as dependent parameters. Scenario 1 assumes a dark asteroid with intensity ranging from 0 to 0.5. Scenario 2 assumes an asteroid with medium intensity ranging from 0.2 to 0.8. Scenario 3 assumes an asteroid with intensity ranging from 0.5 to 1. Figure 4-6 shows distribution of ACPs for scenarios examined.

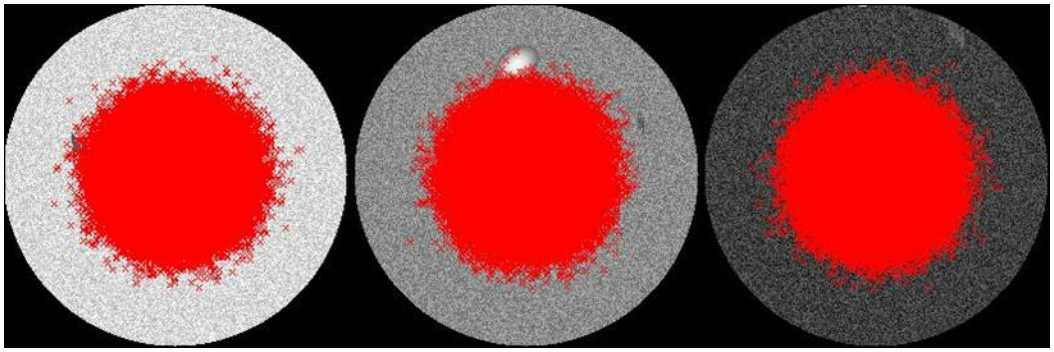

Figure 4-6. Intensity Maps for Light, Mid, and Dark 135 m Radius Asteroid

The respective bond albedo changes are highlighted in Table 4-5. These are calculated through averaging the geometric albedo of every bond albedo change for every particle. As expected, high albedo (white) powder has larger effect for cases of predominately darker surface while low albedo (black) powder should be used for cases of predominately lighter surface. This is assuming 500 m^2 coverage, i.e. 1.4% of the total area.

Table 4-5. Albedo Changes for Several Scenarios.

Scenario	Average Albedo	Modified Average Albedo (White)	Modified Average Albedo (Black)
Light	0.6947	0.7862	0.5795
Mid	0.4228	0.5682	0.3617
Dark	0.2205	0.4276	0.2451

4.3.7 Future Work

A comprehensive range of dispensing velocity variations needs to be evaluated for FF1 and FF2 to plot out accurate distributions of ACPs on the surface. The treatment here was based on particle landing percentages which is a very rudimentary basis for statistical analysis.

A more realistically modeled terrain interface will yield more realistic results. This can be based off of the terrain information from more well-known asteroids such as that of Itokawa. Lastly, the asteroid rotation needs to be taken into account for one rotation if the spacecraft is to paint a band. However, as will be seen by the next section, a band may not be necessary.

4.4 Optimal Dispensing Location

4.4.1 Theory Overview

The optimal dispensing location code here assumes force and torque based on mostly uniform thermal emission; it does not claim to be a rigorous simulation of the Yarkovsky effect since the Yarkovsky effect requires detailed simulation of the surface and subsurface thermal distribution and transfer. There are two main aspects that have to be considered in deciding the area to be sprayed. They are

1. Effective: The area to be sprayed on the asteroid should have a fairly good exposure to the sun. While calculating the area to be sprayed it is usually assumed that the surface of the asteroid is uniformly lit, while in actuality it may so happen that some of the regions receive more sunlight and for a longer period of time then other. This will depend on the inclination of the spin axis of the asteroid and its orbit around the sun.
    a. The asteroid is assumed to be at some location in its orbit. The variation of the asteroid's spin axis orientation needs to be examined.

b. The asteroid will be oriented differently at different points in its orbit. The orbital parameters of the orbit of the asteroid have some variability and need to be examined. Certain regions of the asteroid may receive substantial amounts of sunlight throughout the orbit while other areas vary greatly in amount of sunlight coverage.

2. Convenience: For spraying the asteroid the spacecraft has to hover about the asteroid closely to the surface. This is difficult and rather challenging. Onboard the spacecraft a limited supply of fuel motivates one to considered regions which are easier to paint due to ease in spacecraft hovering about them.

The effective areas are first identified and then are narrowed further by the convenience criterion. The orbit revolution discussed in 1b is ignored for the present analysis. The asteroid is modeled by a randomly generated polyhedron composed of a mesh of tetrahedrons formed from a given ellipsoid of certain radius R. Each surface is a triangle of random shape and area with a random normal vector N. The vector $R_s = [100]$ is assumed to be the normal vector from the sun to the asteroid's center with an asteroid tilt axis of $\pi/6$. The rotation rate is presumed to be a constant $5 * 10{-}3$ rotations/second which translates to a period of .35 hours.

A circular region of 0.5% of the asteroid surface area is defined to be the area of interest. The total force and torque over one rotation of the asteroid is calculated for every combination of triangles that adds up to the surface area. The optimal locations are the combination of areas that yield the largest torque over one revolution.

The algorithm followed can be described in the following steps:

1. Generate a random asteroid of radius *r* or load an asteroid of radius *r*.
2. Acquire the three vectors that describes the x-y-z positions of the *i*th triangular surface and find its centroid.
3. Find the normal vector *N* and the normalized force vector *f* of the *i*th triangular surface.
4. Find the area vector *dA* of the *i*th triangular surface. Considering that the area to be covered is a constant circle while the triangular surfaces are of varying sizes, a method was used to find the intersection area of the circle and the triangle.
5. Knowing the normal vector, normalized force vector, and the area vector, find the forces, torques and normalized torques of the ith triangular surface.
6. Repeat steps 2-4 for all surfaces to account for all surfaces. For each surface, there is a different radius vector, normal vector *N*, and area vector *dA*.
7. Repeat steps 2-5 for all time steps in one orbit. Sum up the forces, torques, and normalized torques.
8. Find the combinations of surfaces that give the area required to be covered and produce the maximum torques and normalized torques in *x*, *y*, and *z* direction.

The amount of torque for each grid is defined as seen in Equation 28 (Rubincam, 2000).

$$d\tau = \vec{r}\, x\, \vec{f}\, \vec{dA} \tag{28}$$

where the normalized force f is calculated in Equation 29 (Rubincam, 2000).

$$\vec{f} = \frac{-2(\hat{R}_s \cdot \hat{N})F_s\hat{N}}{3c} \tag{29}$$

c is the speed of light and F_s is the solar intensity defined as $F_s = \sigma T^4$ where σ is the Stefan-Boltzmann constant. Though the temperature T does vary across the body, for this preliminary study, T is presumed to be a constant 400 K for the sunlit portions and 250 K for the dark portions. Note that modeling the Yarkovsky effect will require a full temperature profile which this study did not attempt to do. The code implemented simply identified surface(s) where a change in thermal emission produces the greatest change in force and torque.

It is considered that a hovering maneuver can be performed to paint the asteroid. The methods to hover have been explored by Broschart and Scheeres (Broschart and Scheeres, 2005). There are two kinds of hovering: Inertial and body fixed. For painting the asteroid body, both types of hovering need to be considered depending on the locations of the most effective areas. Fixed hovering is more useful for large areas concentrated at one location while inertial hovering is more useful for smaller areas distributed over the surface of the asteroid.

The equations for a system in uniformly rotating, body-fixed Cartesian coordinate frame with origin at body's center of mass and rotating uniformly about the x-axis are

$$\ddot{x} = \frac{\partial V}{\partial x} + T_x \tag{30}$$

$$\ddot{y} - 2\omega\dot{z} = \frac{\partial V}{\partial y} + T_y + \omega^2 y \tag{31}$$

$$\ddot{z} + 2\omega\dot{y} = \frac{\partial V}{\partial z} + T_z + \omega^2 z \tag{32}$$

Under body-fixed hovering, the spacecraft's position remains fixed relative to the rotating small-body when placed at nominal hovering point, r0 = [x0, y0, z0]^T. This thrust is defined in Equation 33.

$$T = [-\frac{\partial V}{\partial x}, -\frac{\partial V}{\partial y} - \omega^2 y, -\frac{\partial V}{\partial z} - \omega^2 z]^T \tag{33}$$

A desirable point to hover in terms of fuel will be where the required thrust is a minimum. This will be at a certain attitude above the area of interest that minimizes the cost function of simply ||T||.

For the inertial hovering, the paint sensor/satellite can be tilted to align itself to the spin axis of the asteroid. This is done to avoid unequal distribution of paint particles on the surface of the asteroid. Inertial hovering cost for each grid patch can be calculated in order to find the most suitable patch to paint in terms of fuel. This is done in order to study the trade-off between fuel and effectiveness of the painted area. Broschart and Scheeres in their paper give the thrust required to do a near inertial hovering about an asteroid. If the dynamics of the spacecraft around the asteroid is given the two body equations with spacecraft having negligible mass, then the thrust required to hover at a point in space is given by Equation 34.

$$T(t) = [-\frac{\partial V}{\partial x}, -\frac{\partial V}{\partial y}, -\frac{\partial V}{\partial z}]^T \tag{34}$$

These partial derivatives are evaluated at $r_0(t)$ defined in Equation 35.

$$r_0(t) = \|r_0(0)\|[sin(\lambda_0)cos(\lambda_0)cos(\omega t + \theta_0)cos(\lambda_0)sin(\omega t + \theta_0)]^T \tag{35}$$

Here λ_0 is the initial latitude and θ_0 is the initial longitude at which the spacecraft hovers. The distance from the center is given by $z = \|r_0(0)\|sin(\lambda_0)$. For a constant distance from the center we can calculate the cost of hover for each grid points. A desirable point to hover in terms of fuel will be where the required thrust is minimized. Since the spacecraft will not practically start painting as soon as it hovers, it needs to wait for the targeted patch to come. Therefore, an average cost of hovering is taken over an entire rotation of the asteroid. This implies that the cost of hover is now a function of λ_0 and distance d.

The cost function is defined as seen in Equation 36.

$$J_{fuel} = \oint_0^{2\pi/\omega} T(t)dt \tag{36}$$

Total cost which will decide which grid to paint is given by Equation 37.

$$J = w_1 J_{fuel} + w_2 J_{ref} \tag{37}$$

4.4.2 Results and Discussion

A graphical output of the original case of T = 400K is shown in Figure 4-7.

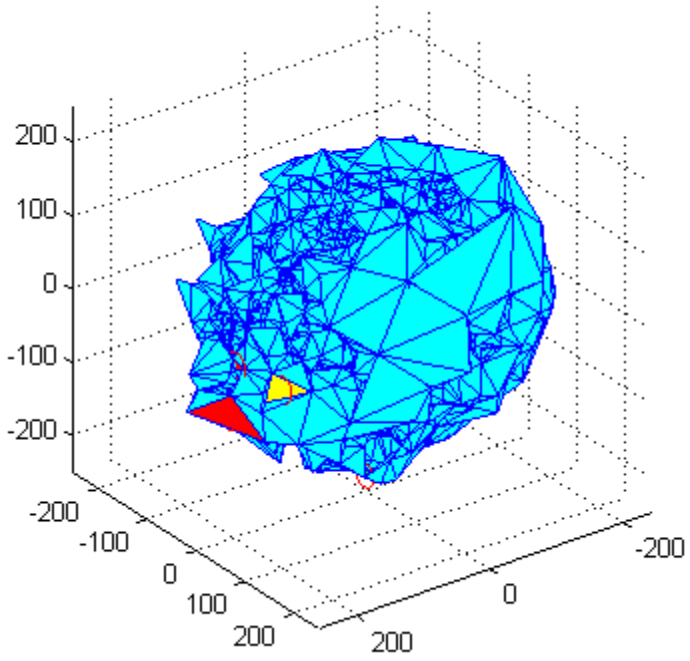

Figure 4-7. Polyhedron Model of Asteroid. The red faced colors indicate the surface to be painted for maximum torque along the x-axis. The yellow faced color indicates that for the maximum torque along the y-axis. The green faced color indicates that for the maximum torque along the z-axis.

The algorithm was run for the range of surface temperatures on the sunlit side from T = 350K to T = 450K. This range was chosen based on knowing the estimate of the sunlit side of the asteroid's average surface temperature to be 400K at 1 AU from the sun (Delbo et al., 2009). The dark side temperature is assumed to be 150K lower than the daytime temperature.

The results for each direction of the forces, normalized torque and torque cases ranging with surface temperatures are shown in Figures 4-8, 4-9, and 4-10 respectively.

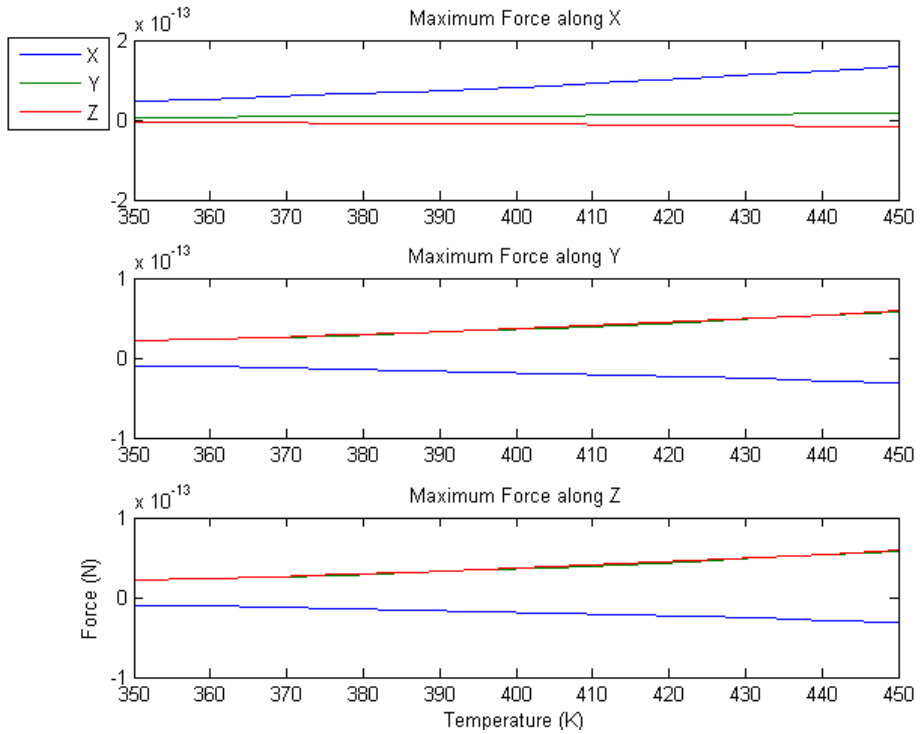

Figure 4-8. Maximum Force vs. Temperature Plot.

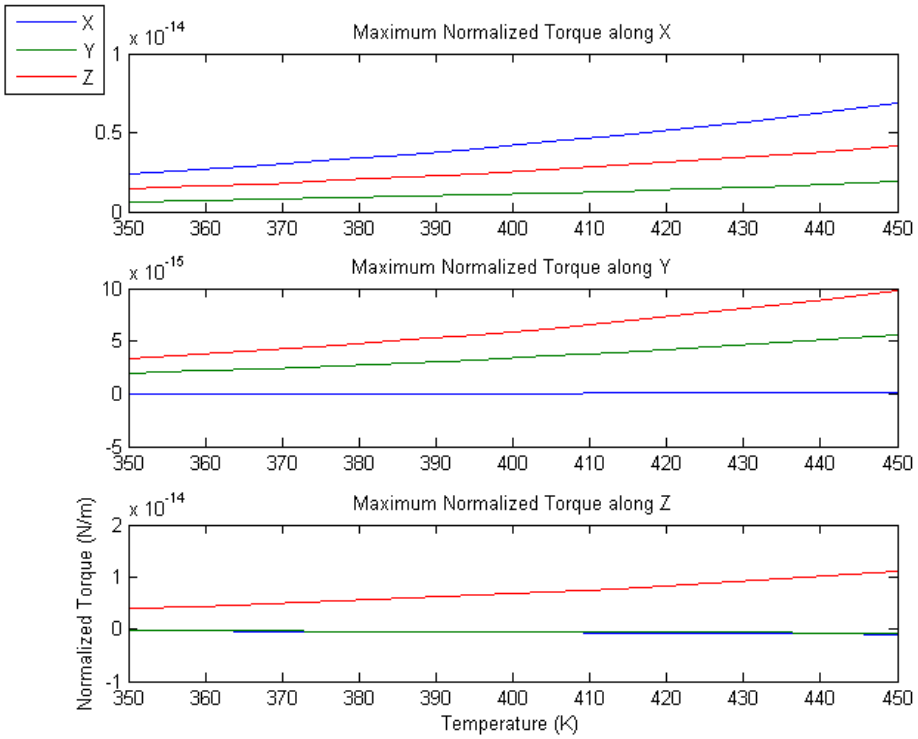

Figure 4-9. Maximum Normalized Torque vs. Temperature Plot.

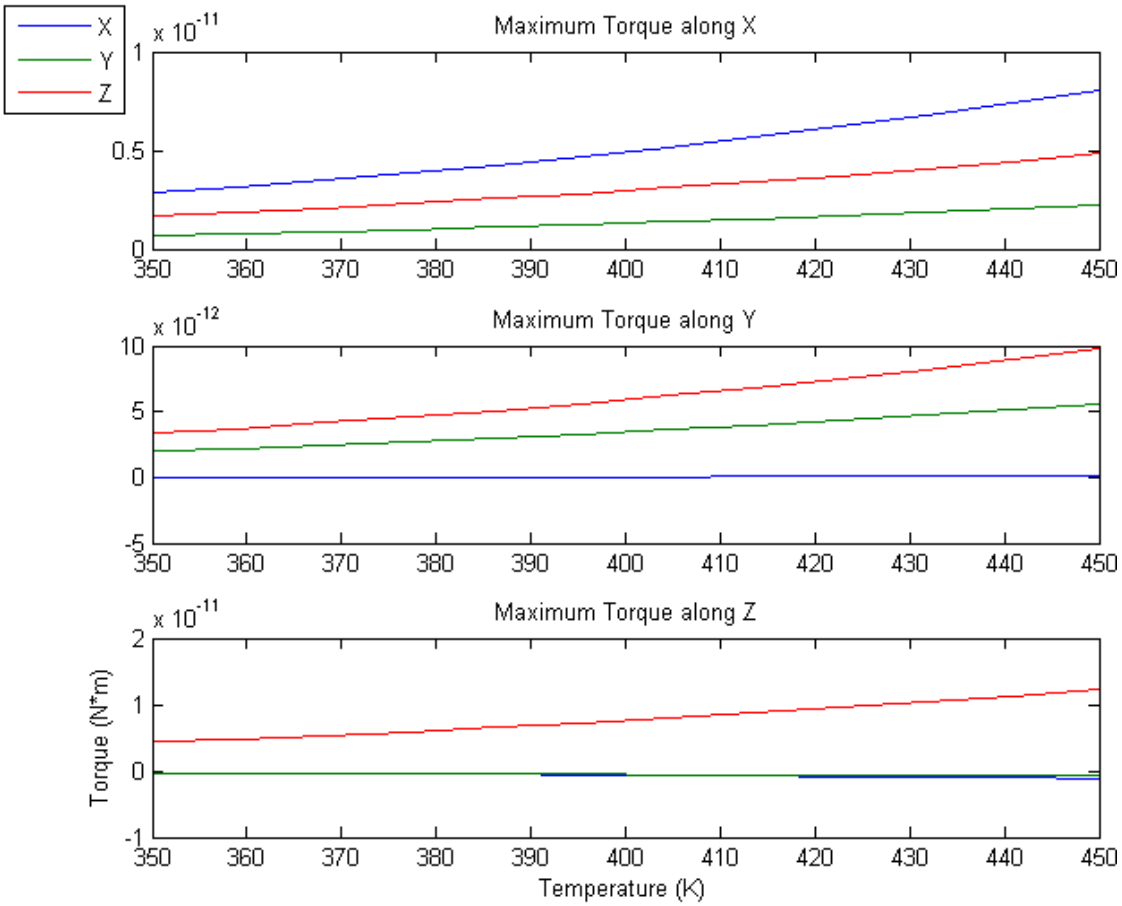

Figure 4-10. Maximum Torque vs. Temperature Plot.

As expected by Equation 29, higher temperature results in greater torque. The numbers also match nicely with the quartic rise calculated by the formula, i.e. the torque at 450 K is approximately (450/350)4 = 2.7326 times greater than that of the torque at 350 K. However, since about a hundred of known near-earth asteroids and probably many more have perihelion distances below 0.3 AU where sunlit surface temperatures can rise above 800K, especially in craters, and knowing the proportional rate to be correct, a derivation shows that the torque at 450 K will be 27 times greater than at 350 K (Delbo et al., 2009).

The algorithm was also run for the range of axis tilts from $\theta = 0$ to $\theta = \pi/2$. Considering the solar rays to the center of the asteroid are incident from [100] and the tilt axis for rotation at 90 degrees is exactly coincident with it, the torque generated at 90 degrees should be smallest since the surface area exposed to the sun over one rotation remains mostly uniform there. This is exactly as observed and O (10^6) ratio in torque difference is observed between maximum torque at 0 degrees and minimum torque at 90 degrees. The results for the force, normalized torque and torque cases are shown in Figures 4-11, 4-12 and 4-13 respectively.

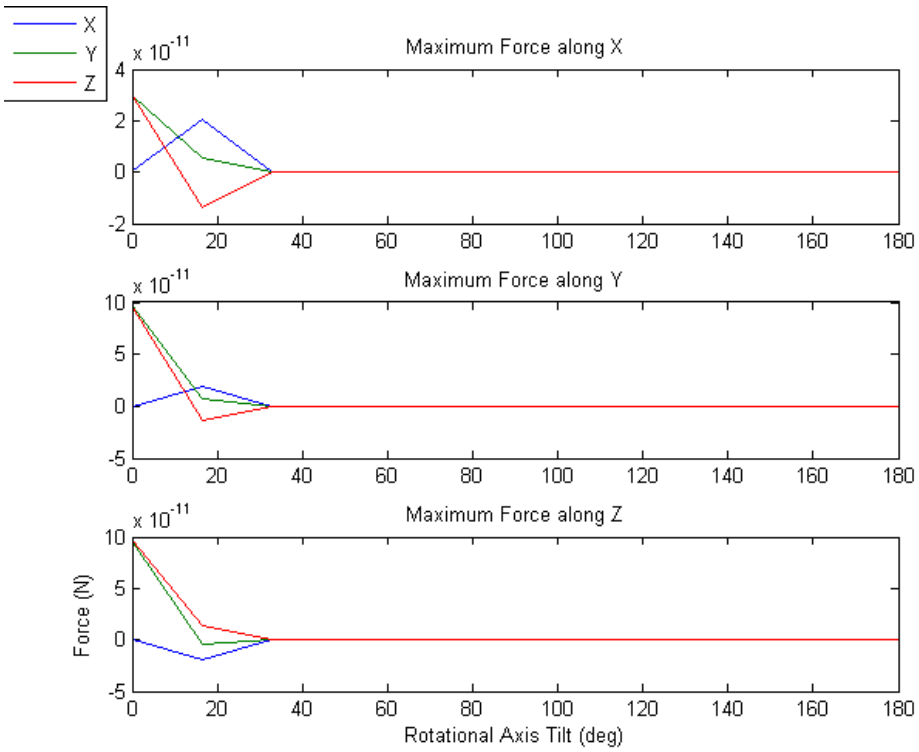

Figure 4-11. Maximum Force vs. Tilt Angle.

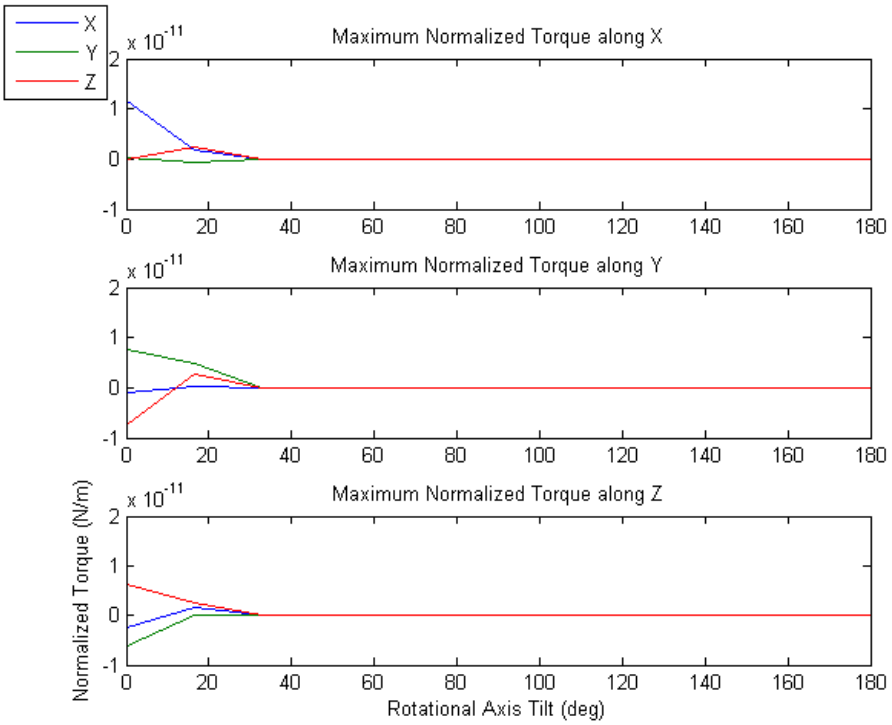

Figure 4-12. Maximum Normalized Torque vs. Tilt Angle.

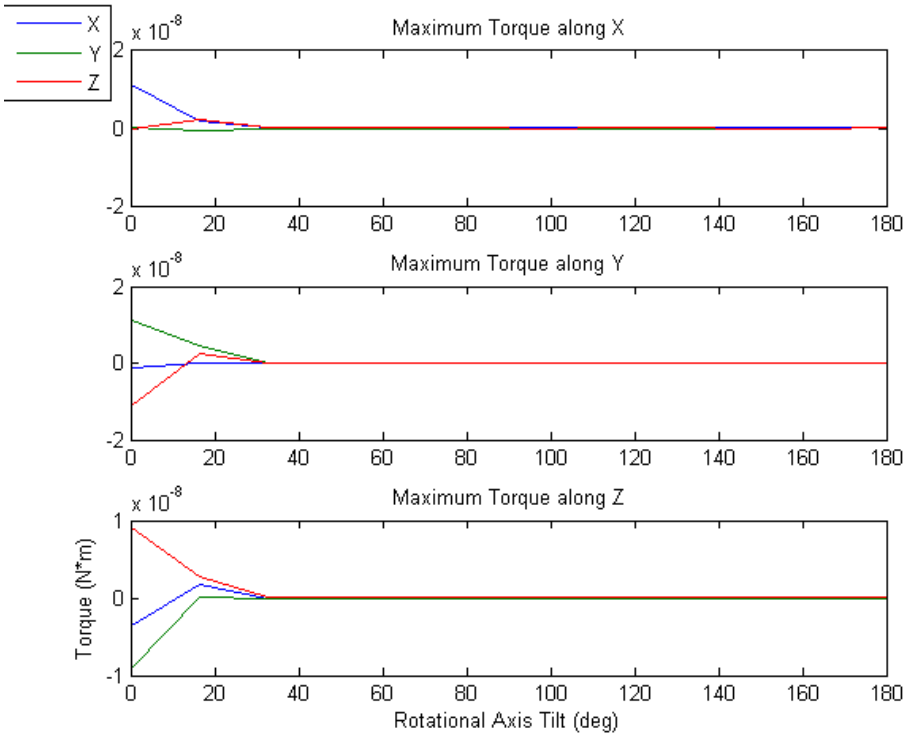

Figure 4-13. Maximum Torque vs. Tilt Angle.

4.4.3 Force or Torque

The significance of the torque primarily depends on the orbit of the body and the shape of the body (Rubincam, 2007). An elliptical orbit is crucial for the torque on semimajor axis and orbital ellipticity vanishes for a circular orbit regardless of the asteroid's shape or spin axis orientation as can be seen in Figure 4-14.

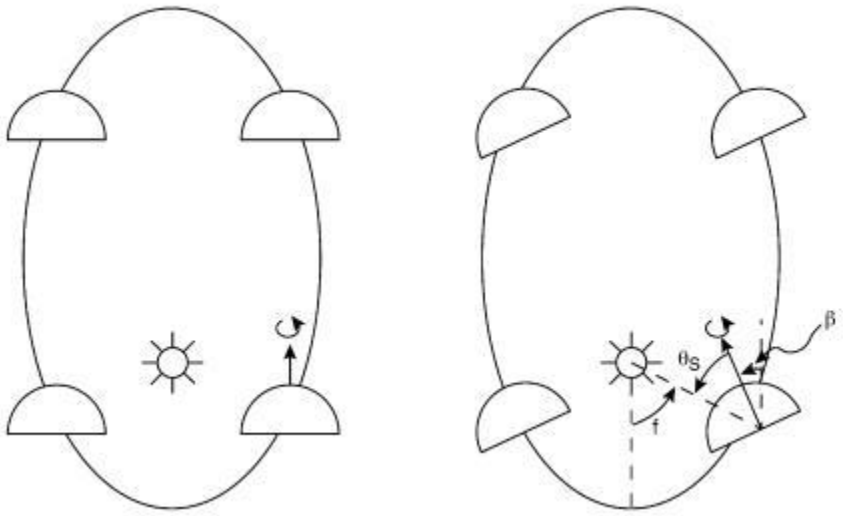

Figure 4-14. Quasi-secular Orbit Evolution. The spin axis is in the plane of the orbit. Left: The spin axis is parallel to the long axis of the ellipse. Right: The spin axis is tilted by an angle β with respect to the axis of the ellipse. The broken symmetry results in a quasi-secular orbit evolution. The angle f is the true anomaly (Rubincam, 2007).

Rubincam has shown in his paper that assuming Apophis's density to be 2800 kg/m3 yields a quasi-secular effect which averages out to zero on O(1000 years) due to orbit and spin axis precession that averages out to 0. However, torque effect in semimajor axis is large enough to allow Apophis to possibly go through the keyhole. The amount that torque can affect along the along-track decision is found in Equation 38.

$$\Delta d = 0.61325 sin(\beta)[T(yr)]^2 km \tag{38}$$

For T (yr) 20yr, $\Delta d = 245 sin(\beta)$ km which is comparable to ±250 km for the Yarkovsky force derived by Chesley. However, as Rubincam pointed out, this is a very optimistic outlook since the shape model Rubincam used to derive his estimate was a perfect hemisphere which maximized the torque and he assumed the night side temperature to be at absolute zero.

Another concern is whether thermal emission and gravity will torque the asteroid enough causing sufficient precession that β will significantly change. For Apophis, Rubincam's equation showed that the two are comparable as seen in Equation 39. If R_A = 135 m, the torques are equal if ρ = 1200 kg/m^3 which is a good model for a half-empty stony rubble-pile. Considering that the solar gravitational torque is negligible, the torque from thermal emission is also negligible.

$$\frac{N_{YORP}}{N_{grav}} = \frac{2.36 * 10^7}{\rho R_A^2} \frac{a}{a_E} \tag{39}$$

Overall, the torque appears to be much less significant than the force from thermal emission.

4.4.4 Thoughts

A look at the distribution of maximum force and torque areas show that one large area is preferred over lots of smaller areas. This means that body-fixed hovering for this model works better than inertial hovering considering the limited distribution of necessary coverage. The optimal hovering altitude remains to be found. There is much to

be investigated beyond this point as well. The orbital parameters changes were not examined. Future studies will entail a variation of those parameters. Factors that will change due to the orbit will include:

1. Radial vector R_s from the sun to the asteroid
2. Distance from the sun to the asteroid will affect the temperature of the surface. Presumably, at periapsis, the temperature will be greatest.
3. Orientation of the orbital plane will change the spin axis relative to the sun

Furthermore, additions to the model are necessary for a more realistic model:

1. Orientation of the spin axis along all possible directions
2. Location of the center of mass of the asteroid
3. Thermal distribution of asteroid surface

The thermal distribution of the asteroid surface was assumed to be uniform. Though this does not affect the YORP effect, the Yarkovsky effect is dependent on temperature variation across the surface. This will have to be rectified in the future. One possibility is using Rubincam's model (Rubincam, 1995) in Equation 40.

$$\Delta T \propto [1 + 2\Phi + 2\Phi^2]^{-\frac{1}{2}} \tag{40}$$

The thermal parameter Φ is defined as in Equation 41.

$$\Phi = \frac{2\Gamma\sqrt{\omega}}{\epsilon\sigma T^3} \tag{41}$$

where thermal inertia Γ is defined as $\Gamma = \sqrt{k\rho c}$. Note that is the emissitivity of the surface, k is the thermal conductivity of the surface, c is the thermal capacity of the

surface, and ρ is the surface density. Taking these into consideration will produce a non-uniform temperature across the asteroid surface which will produce a more realistic Yarkovsky and YORP effect.

5. CONCLUSION

I envisioned the original concept of modifying the terrestrial industrial electrostatic dispenser system for modification of surface albedo of asteroids. The design and implementation of a payload (SATS) to mitigate the near earth asteroid threat has been discussed from both experimental and simulation perspectives. The anticipated implementation of SATS on a real mission to Apophis and the final proof of its effectiveness before the end of this decade is a goal that the work presented in this document has paved the way for.

The project remains active and presents continual challenges that only a team effort can propel to success. This will continue with the beginning of actual ground experiment testing and the development of the LEO satellite for flight testing with international collaboration from KACST (King Abdulaziz City for Science and Technology).

REFERENCES

Badhwar, G. D., 1997. Radiation Environment in Low-Earth Orbit. Radiation Research, 148 (5), S3-S10.

Biller, K., 2009. (kevinbiller@yahoo.com). "Some Questions." Personal Communication.

Biller, K., 2010. (kevinbiller@yahoo.com). "Texas A&M: On Contract Progress." Personal Communication.

Binzel, R., Rivkin, A., Thomas, C., Vernazza P., Burbine, T., DeMeo, F., Bus, S., Tokunaga, A., Birlan, M, 2009. Spectral Properties and Composition of Potentially Hazardous Asteroid (99942) Apophis. Icarus 200, 480-485.

Bottke Jr., W., Vokrouhlický D., Rubincam, D., Broz, M., 2002. Effect of Yarkovsky Thermal Forces on the Dynamical Evolution of Asteroids and Meteoroids. Asteroids III. Univ. of Arizona Press: Tucson, 395-408.

Broschart, S.B., Scheeres, D.J., 2005. Control of Hovering Spacecraft Near Small Bodies: Application to Asteroid 25143 Itokawa. Journal of Guidance, Control, and Dynamics, 28 (2), 343-354.

Burns, J. A., 1979. Radiation Forces on Small Particles in the Solar System. Icarus 40, 1-48.

Cheever, G. D., 1975. Electrostatic Charge Acceptance and Decay of Powder Coating Particles. Journal of Applied Polymer Science, 19, 147-163.

Dascalescu, L., 2005. Virtual Instrument for Statistic Control of Powder Tribo-charging Processes. Journal of Electrostatics, 63, 565-570.

Dascalescu, L., 2009. (lucian.dascalescu@univ-poitiers.fr). "Questions." Personal Communication.

Dascalescu, L., Medles, K., Das, S., Younes, M., Caliap, L., and Mihalcioiu, A., 2008. Using Design of Experiments and Virtual Instrumentation to Evaluate the Tribocharging of Pulverulent Materials in Compressed-Air Devices. IEEE Transactions on Industry Applications, 44 (1), 3-8.

Dascalescu, L., Bilici, M., Chereches, R., 2010. Triboelectric Phenomena in Suction-Type Dilute-Phase Pneumatic Transportation Systems for Granular Plastics. IEEE Transactions on Industry Applications, 46 (4), 1570-1577.

Delbo, M., Marchi, S., Morbidelli, A., 2009. Temperature Stress at the Surface of Near-Earth Asteroids. 72nd Annual Meteoritical Society Meeting. Meteoritics and Planetary Science Supplement, Nancy, 5272.

Giorgini, J., Benner, L., Ostro, S., Nolan, M., Busch, M., 2008. Predicting the Earth Encounters of (99942) Apophis. Icarus 193, 1-19.

Greason, W., Oltean, I., Kucerovsky, Z., Ieta, A., 2004. Triboelectric Charging Between Polytetrafluoroethylene and Metals. IEEE Transactions on Industry Applications, 40 (2), 442-450.

Gueymard, C.A., 2004. Sun's Total and Spectral Irradiance for Solar Energy Applications and Solar Radiation Models. Solar Energy 76, 423-453.

Han, J.H., Kim, C.G., 2006. Low earth orbit space environment simulation and its effects on graphite/epoxy composites. Composite Structures 72, 218-226.

Hyland, D.C., Altwaijry, H.A., Ge, S., Margulieux, R., Doyle, J., Sandberg, J., Young, B., Bai, X., Lopez, J., Satak, N., 2009. A Permanently-Acting NEA Mitigation Technique via the Yarkovsky Effect. Cosmic Research, 48 (5), 430-436.

Komatsu, T., Masuda, H., Iinoya, K., 1976. Static Electrification of Particles in Gas-Solids Pipe Flow. AlChe Journal 22 (3), 558-564.

Lee, P., 1996. Dust Levitation on Asteroids. Icarus 124, 181-194.

Li, Z., Zhang C., Zhu, J., 2005. Numerical Study of the Effect of Particle Size on the Coating Efficiency and Uniformity of an Electrostatic Powder Coating Process. Canadian Journal of Chemical Engineering, 83, 882-888.

Mayr, M. B., Barringer, S.A., 2006. Corona Compared with Triboelectric Charging for Electrostatic Powder Coating. Journal of Food Science, 71, E171-E177.

Miyamoto, H., Yano, H., Scheeres, D., Abe, S., Barnouin-Jha, O., et al., 2007. Regolith Migration and Sorting on Asteroid Itokawa. Science 316, 1011-1014.

Mountain, J.R., 2010. Personal Communication.

Mountain, J.R., Mazumder, M.K., 2001. Triboelectric Charging of Polymer Powders in Fluidization and Transport Processes. IEEE Transactions on Industry Applications, 37 (3), 778-784.

Mihalcioiu, A., Dascalescu, L., Das, S., Medles, K., Munteanu, R., 2005. Virtual Instrument for Statistic Control of Powder Tribo-charging Processes. Electrostatics 63, 565-570.

Murnane, S., Barnes, R., Woodhead, S., Amadi-Echendu, J., 1996. Electrostatic Model ling and Measurement of Airborne Particle Concentration. IEEE Transactions on Instrumentation and Measurement, 45 (2), 488-492.

Nitter, T., Havnes, O., 1992. Dynamics of Dust in a Plasma Sheath and Injection of Dust into the Plasma Sheath above Moon and Asteroidal Surfaces. Earth, Moon, and Planets, 56, 7-34.

Poppe, T., Schrapler, R. 2005. Further Experiments on Collisional Tribocharging of Cosmic Grains. Astronomy and Astrophysics, 438, 1-9.

Reddy, M. R., 1995. Review Effect of Low Earth Orbit Atomic Oxygen on Spacecraft Materials. Journal of Materials Science, 30, 281-307.

Rubincam, D.P, 1995. Asteroid Orbit Evolution due to Thermal Drag. Journal of Geophysical Research 100, 1585-1594.

Rubincam, D.P., 2000. Radiative Spin-up and Spin-Down of Small Asteroids. Icarus 148, 2-11.

Rubincam, D.P., 2007. Orbital YORP and Asteroid Orbit Evolution, with Application to Apophis. Icarus 192, 460-468.

Schweickart, R., Chapman C., Durda D., Hut, P., Bottke, B., Nesvorn, D., 2006. Threat Characterization: Trajectory Dynamics. NASA Workshop on Near-Earth Objects. Vail, Colorado.

Shah, U., Zhang, C., Zhu, J., 2005. Comparison of Electrostatic Fine Powder Coatings and Coarse Powder Coatings by Numerical Simulations. Electrostatics 64, 345-354.

Smith, W. A. P., Hancock, E.R., 2005. Single Image Estimation of Facial Albedo Maps. Brain, Vision, and Artificial Intelligence 3704, 517-526.

Sola, Y., Ortiz, A., Lorente, J., 2007. Influence of Extraterrestrial Spectrum on the Modeled UV Irradiance. UV Conference. Davos, Switzerland.

Supuk, E., Siler, C., Mojtaba, G., 2009. Analysis of a Simple Test Device for Tribo-electric Charging of Bulk Powders. Particle Particle System Characteristics, 26, 7-16.

Technovision, 2005. Software Quality Assurance Methodology Series: Test Case Design Using the Taguchi Method. <http://www.qavision.com/expertzone/test_case_design_using_taguchi_method.pdf>

Thomas, A., Khashayar, S., Guigon, P., Czechowski, C., 2007. Tribocharging Behavior of Automotive Powder Coatings. Journal of Physics Conf. Series 142, 1-6.

Vokrouhlický, D., Milani, A., Chelsey, S.R., 2000. Yarkovsky Effect on Small Near-Earth Asteroids: Mathematical Formulation and Examples. Icarus 148, 118-138.

White, C., Roberts, G., Chambers, A., 2005. Measurement of 5-eV Atomic Oxygen Using Carbon Based Films: Preliminary Results. IEEE Sensors Journal, 5 (6), 1206-1213.

APPENDIX A

SIMULATION OUTPUTS

Table A-1. Particle Dispersal Landing Times for Initial Velocities (FF1 165 m). Initial particle velocities and final landing times at top of sheath at 5000 s assuming the spacecraft is at altitude of 150 m and a maximum asteroid radius of 165 m. From 3 cm/s to 15 cm/s, 32.97% particles did not land.

$V_{initial}$ (cm/s)	Φ	t_{land} (s)
3	0	2075
3	π/6	2180
3	π/3	2485
3	π/2	2955
4	0	1940
4	π/6	2065
4	π/3	2450
4	π/2	3080
5	0	1815
5	π/6	1960
5	π/3	2430
5	π/2	3270
6	0	1705
6	π/6	1860
6	π/3	2430
6	π/2	3600
7	0	1600
7	π/6	1775
7	π/3	2450
8	0	1510
8	π/6	1695
8	π/3	2500
9	0	1425
9	π/6	1620
9	π/3	2625
10	0	1350
10	π/6	1550
11	0	1280
11	π/6	1485
12	0	1215
13	0	1155
13	π/6	1370
14	0	1100
14	π/6	1320
15	0	1050
15	π/6	1270

Table A-2. Particle Dispersal Landing Times for Initial Velocities (FF1 135 m). Initial particle velocities and landing times at top of sheath at 5000 s assuming the spacecraft is at an altitude of 150 m and a nominal asteroid radius of 135 m. The percentage of particles that did not land for velocities ejected from 3 cm/s to 15 cm/s is 32.97%.

$V_{initial}$ (cm/s)	Φ	t_{land} (s)
3	0	1980
3	π/6	2075
3	π/3	2360
3	π/2	2790
4	0	1855
4	π/6	1970
4	π/3	2335
4	π/2	2910
5	0	1740
5	π/6	1875
5	π/3	2320
5	π/2	3095
6	0	1640
6	π/6	1790
6	π/3	2330
6	π/2	3445
7	0	1545
7	π/6	1710
7	π/3	2360
8	0	1460
8	π/6	1635
8	π/3	2440
9	0	1380
9	π/6	1570
9	π/3	2670
10	0	1310
10	π/6	1510
11	0	1245
11	π/6	1450
12	0	1185
12	π/6	1400
13	0	1130
13	π/6	1350
14	0	1075
14	π/6	1305
15	0	1030
15	π/6	1260

Table A-3. Particle Dispersal Landing Times for Initial Velocities (FF1 105 m). Initial particle velocities and landing times at top of sheath at 5000 s assuming the spacecraft is at an altitude of 150 m and a nominal asteroid radius of 105 m. The percentage of particles that did not land for velocities ejected from 3 cm/s to 15 cm/s is 35.16%.

$V_{initial}$ (cm/s)	Φ	t_{land} (s)
3	0	1860
3	π/6	1950
3	π/3	2210
3	π/2	2590
4	0	1750
4	π/6	1855
4	π/3	2190
4	π/2	2705
5	0	1650
5	π/6	1775
5	π/3	2185
5	π/2	2885
6	0	1555
6	π/6	1700
6	π/3	2200
6	π/2	3250
7	0	1475
7	π/6	1630
7	π/3	2250
8	0	1395
8	π/6	1565
8	π/3	2365
9	0	1325
9	π/6	1505
10	0	1260
10	π/6	1455
11	0	1200
11	π/6	1405
12	0	1145
12	π/6	1360
13	0	1090
13	π/6	1315
14	0	1045
14	π/6	1280
15	0	1000
15	π/6	1240

Table A-4. Particle Dispersal Landing Locations for Initial Velocities (FF2 165 m). Initial particle velocities and the final z-positions on the surface of the asteroid assuming the spacecraft is at an altitude of 150 m with sheath height of 1 m and a nominal asteroid radius of 165 m for varying solar wind Mach numbers and normalized sheath potential at 1 m. The x and y-positions are for $\theta = 0$. Any particle that did not penetrate the sheath is not shown. Since there's negligible different between Mach numbers and sheath potential, only the extreme cases are shown here.

Mach	Potential	V (cm/s)	ϕ	x (m)	y (m)	z (m)
0.95	-3	8	$-\pi/6$	63.6807	0	153.1076
0.95	-3	8	0	-56.0377	0	156.0674
0.95	-3	8	$\pi/6$	-63.6807	0	153.1076
0.95	-3	9	$-\pi/6$	64.7143	0	152.6672
0.95	-3	9	0	-56.5100	0	155.8908
0.95	-3	9	$\pi/6$	-64.7143	0	152.6672
0.95	-3	10	$-\pi/6$	63.1084	0	153.3320
0.95	-3	10	0	-56.5780	0	155.8599
0.95	-3	10	$\pi/6$	63.1084	0	153.3320
0.95	-3	11	$-\pi/6$	63.4814	0	153.1716
0.95	-3	11	0	-56.2444	0	155.9744
0.95	-3	11	$\pi/6$	-63.4814	0	153.1716
0.95	-3	12	$-\pi/6$	63.5509	0	153.1363
0.95	-3	12	0	-55.5021	0	156.2340
0.95	-3	12	$\pi/6$	-63.5509	0	153.1363
0.95	-3	13	$-\pi/6$	63.3191	0	153.2259
0.95	-3	13	0	-54.3330	0	156.6382
0.95	-3	13	$\pi/6$	-63.3191	0	153.2259
0.95	-3	14	$-\pi/6$	65.3880	0	152.3476
0.95	-3	14	0	-56.2046	0	155.9698
0.95	-3	14	$\pi/6$	-65.3880	0	152.3476
0.95	-3	15	$-\pi/6$	64.6448	0	152.6581
0.95	-3	15	0	-54.3212	0	156.6296
0.95	-3	15	$\pi/6$	-64.6448	0	152.6581
5	-4.1	8	$-\pi/6$	63.6805	0	153.1070
5	-4.1	8	0	-56.0375	0	156.0668
5	-4.1	8	$\pi/6$	-63.6805	0	153.1070
5	-4.1	9	$-\pi/6$	64.7140	0	152.6666
5	-4.1	9	0	-56.5098	0	155.8902
5	-4.1	9	$\pi/6$	-64.7140	0	152.6666
5	-4.1	10	$-\pi/6$	63.1081	0	153.3314
5	-4.1	10	0	-56.5778	0	155.8593
5	-4.1	10	$\pi/6$	-63.1081	0	153.3314
5	-4.1	11	$-\pi/6$	63.4811	0	153.1710
5	-4.1	11	0	-56.2442	0	155.9738
5	-4.1	11	$\pi/6$	-63.4811	0	153.1710
5	-4.1	12	$-\pi/6$	63.5507	0	153.1357
5	-4.1	12	0	-55.5018	0	156.2333
5	-4.1	12	$\pi/6$	-63.5507	0	153.1357
5	-4.1	13	$-\pi/6$	63.3188	0	153.2253
5	-4.1	13	0	-54.3328	0	156.6376
5	-4.1	13	$\pi/6$	-63.3188	0	153.2253
5	-4.1	14	$-\pi/6$	65.3878	0	152.3470
5	-4.1	14	0	-56.2044	0	155.9691
5	-4.1	14	$\pi/6$	-65.3878	0	152.3470
5	-4.1	15	$-\pi/6$	64.6446	0	152.6574
5	-4.1	15	0	-54.3210	0	156.6289
5	-4.1	15	$\pi/6$	-64.6446	0	152.6574

Table A-5. Particle Dispersal Landing Locations for Initial Velocities (FF2 135 m). Initial particle velocities and final positions on the surface of the asteroid assuming the spacecraft is at an altitude of 150 m with sheath height of 1 m and a nominal asteroid radius of 135 m for normalized sheath potential at 1 m. The x and y-positions are for $\theta = 0$. Any particle that did not penetrate the sheath is not shown. Since there's negligible different between Mach numbers and sheath potential, only the extreme cases are shown here.

Mach	Potential	$V_{initial}$ (cm/s)	Φ	x (m)	y (m)	z (m)
0.95	-3	14	0	80.18	0	109.6
0.95	-3	15	$-\pi/6$	-81.55	0	108.6
0.95	-3	15	0	-46.43	0	127.6
0.95	-3	15	$\pi/6$	81.55	0	108.6
5	-4.1	14	0	80.18	0	109.6
5	-4.1	15	$-\pi/6$	-81.55	0	108.6
5	-4.1	15	0	-46.43	0	127.6
5	-4.1	15	$\pi/6$	81.55	0	108.6

Table A-6. Particle Dispersal Landing Locations for Initial Velocities (FF2 105 m). Initial particle velocities and the final positions on the surface of the asteroid assuming the spacecraft is at an altitude of 150 m with sheath height of 1 m and a minimum asteroid radius of 105 m. The x and y-positions are for θ = 0. Any particle that did not penetrate the sheath is not shown.

Mach	Potential	V (cm/s)	ϕ	x (m)	y (m)	z (m)
0.95	-3	9	0	104.2344	0	18.2737
0.95	-3	10	0	82.1321	0	66.7327
0.95	-3	11	$-\pi/6$	-83.2006	0	65.3896
0.95	-3	11	0	-72.0218	0	77.5331
0.95	-3	11	$\pi/6$	83.2006	0	65.3896
0.95	-3	12	$-\pi/6$	-84.3768	0	63.8578
0.95	-3	12	0	-72.0927	0	77.4617
0.95	-3	12	$\pi/6$	84.3768	0	63.8578
0.95	-3	13	$-\pi/6$	-85.1947	0	62.7558
0.95	-3	13	0	-71.5532	0	77.9555
0.95	-3	13	$\pi/6$	85.1947	0	62.7558
0.95	-3	14	$-\pi/6$	-86.6708	0	60.6922
0.95	-3	14	0	-71.9145	0	77.6159
0.95	-3	14	$\pi/6$	86.6708	0	60.6922
0.95	-3	15	$-\pi/6$	-87.3651	0	59.6809
0.95	-3	15	0	-71.7648	0	77.7484
0.95	-3	15	$\pi/6$	87.3651	0	59.6809
5	-4.1	9	0	104.2337	0	18.2736
5	-4.1	10	0	82.1316	0	66.7323
5	-4.1	11	$-\pi/6$	-83.2001	0	65.3892
5	-4.1	11	0	-72.0214	0	77.5326
5	-4.1	11	$\pi/6$	83.2001	0	65.3892
5	-4.1	12	$-\pi/6$	-84.3763	0	63.8574
5	-4.1	12	0	-72.0922	0	77.4612
5	-4.1	12	$\pi/6$	84.3763	0	63.8574
5	-4.1	13	$-\pi/6$	-85.1941	0	62.7554
5	-4.1	13	0	-71.5527	0	77.955
5	-4.1	13	$\pi/6$	85.1941	0	62.7554
5	-4.1	14	$-\pi/6$	-86.6703	0	60.6918
5	-4.1	14	0	-71.914	0	77.6154
5	-4.1	14	$\pi/6$	86.6703	0	60.6918
5	-4.1	15	$-\pi/6$	-87.3645	0	59.6806
5	-4.1	15	0	-71.7643	0	77.7479
5	-4.1	15	$\pi/6$	87.3645	0	59.6806

APPENDIX B

EQUIPMENT LIST AND SUPPLIES

Table B-1. Supply List of Equipment for Ground Experiment.

Equipment	Quantity	Cost (unit)
Helium	N/A	$0.20/cubic ft
Helium Tank	2	$10.00
2-stage Regulator	2	$25.00
Air Compressor	1	$200.00
Air Filter	1	$25.00
Infrared Heaters	1	$354.50
Thermistor	10	$3.50
Shimadzu Scales	2	$1175.00
PC	1	$1000.00
Imperx Camera	1	$3593.50
Micro-Nikkor Nikon Lens	1	$1062.37
Macro Tilt Adapter	1	$94.90
C-Mount Adapter	1	$33.30
Logitech PRO 9000	1	$79.99
EPIX Frame Grabber	1	$570.00
Aluminum Sheet (24x18)	2	$18.42
6V Battery	2	$3.87
Multimeter	1	$26.97
Wire/Alligator clip	1	$4.30
Spray Booth	1	$222.00
UV-IR Source	1	$40.00

Table B-2. Trade-off Study of Tribodispensers. The Nordson Tribomatic 500 was chosen for ground experiment.

Company	Cost (unit)	Customer Support	Ease of Use
itwGewa	$5795.00	MODERATE	MODERATE
SAMES	$6526.00	LOW	HIGH
Wagner	$4935.00	MODERATE	HIGH
Nordson	$3527.00	HIGH	HIGH

Table B-3. Trade-off Study of Painting Powders. The Arkema Kynar was chosen as the preliminary powder.

Company	Color	Thickness	Temperature
AkzoNobel	LOW	LOW	HIGH
Arkema	HIGH	HIGH	MODERATE
Cardinal	HIGH	LOW	LOW
Chevron Phillips	MODERATE	HIGH	LOW
Dupont	HIGH	MODERATE	MODERATE
Solvay Solexis	LOW	MODERATE	LOW
Tiger Drylac	HIGH	HIGH	LOW
Whitford	LOW	MODERATE	MODERATE

VITA

Name: Shen Ge

Address: Dept of Aerospace Engineering
HRBB 701, Ross Street
TAMU 3141
College Station, TX 77843

Email Address: shenge86@gmail.com

Education: B.S., Aerospace Engineering, Georgia Institute of Technology, 2008
M.S., Aerospace Engineering, Texas A&M University, 2011